



# LHC BUNCH CURRENT NORMALISATION FOR THE APRIL-MAY 2010 LUMINOSITY CALIBRATION MEASUREMENTS

G. Anders<sup>1,2</sup>, N. Bacchetta<sup>2</sup>, V. Balagura<sup>2,3</sup>, C. Barschel<sup>2,4</sup>, D. Belohrad<sup>2</sup>, D. Berge<sup>2</sup>, H. Burkhardt<sup>2</sup>, S.I. Cooper<sup>5</sup>, M. Ferro-Luzzi<sup>2</sup>, G. Franzoni<sup>5</sup>, C. Gabaldon<sup>2</sup>, M. Gagliardi<sup>6</sup>, J.J. Gras<sup>2</sup>, V. Halyo<sup>7</sup>, B. Heinemann<sup>8</sup>, P. Hopchev<sup>9</sup>, A. Hunt<sup>7</sup>, W. Kozanecki<sup>10</sup>, S. Kwan<sup>11</sup>, M. Ludwig<sup>2</sup>, D. Marlow<sup>7</sup>, P. Odier<sup>2</sup>, S. Pagan Griso<sup>8</sup>, J. Panman<sup>2</sup>, T. Pauly<sup>2</sup>, S. Thoulet<sup>2</sup>, S. White<sup>2</sup>, J.C. Yun<sup>11</sup>, and M. Zanetti<sup>12</sup>

<sup>1</sup>Ruprecht-Karls-Universität Heidelberg: Kirchhoff-Institut für Physik, Heidelberg, Germany

<sup>2</sup>CERN, Geneva, Switzerland

<sup>3</sup>Institute of Theoretical and Experimental Physics (ITEP), Moscow, Russia

<sup>4</sup>RWTH Aachen University, III. Physikalisches Institut A, Aachen, Germany

<sup>5</sup>University of Minnesota, Minneapolis, USA

<sup>6</sup>INFN sezione di Torino, Torino, Italy

<sup>7</sup>Princeton University, Princeton, New Jersey, USA

<sup>8</sup>Lawrence Berkeley National Laboratory and University of California, Berkeley, California, USA

<sup>9</sup>LAPP Annecy, France

<sup>10</sup>CEA, DSM/IRFU, Centre d'Etudes de Saclay, FR - 91191 Gif-sur-Yvette, France

<sup>11</sup>Fermi National Accelerator Laboratory, Batavia, Illinois, USA

<sup>12</sup>Massachusetts Institute of Technology, Cambridge, Massachusetts, USA

February 7, 2011

## Abstract

In April-May 2010, a series of experiments were done to perform first luminosity calibration measurements for each LHC Interaction Point at the zero-momentum frame energy  $\sqrt{s} = 7$  TeV. In this note, the results are presented of the LHC bunch current normalization analysis for these experiments. The uncertainties, and the prospects to reduce these for future experiments, are discussed in detail.

## Contents

<b>1</b>	<b>Introduction</b>	<b>3</b>
<b>2</b>	<b>Description of the luminosity calibration measurements</b>	<b>3</b>
<b>3</b>	<b>Description of the BCT systems</b>	<b>4</b>
3.1	The DCCT system . . . . .	5
3.2	The FBCT system . . . . .	5
<b>4</b>	<b>Bunch population data analysis</b>	<b>6</b>
4.1	Total beam population . . . . .	6
4.1.1	DCCT baseline subtraction . . . . .	7
4.1.2	Absolute scale of the DCCT . . . . .	12
4.2	Relative bunch populations . . . . .	13
4.3	Ghost charge and satellite bunches . . . . .	16
4.3.1	Ghost charge from beam-gas interactions . . . . .	17
4.3.2	Satellite bunch populations from precise timing . . . . .	19
4.3.3	Satellite bunch populations from vertexing . . . . .	21
4.3.4	Summary on ghost charge and satellite bunches . . . . .	24
<b>5</b>	<b>Discussion and summary</b>	<b>25</b>
<b>6</b>	<b>Acknowledgements</b>	<b>28</b>
<b>7</b>	<b>Appendix</b>	<b>31</b>

# 1 Introduction

The ability to measure luminosity on an absolute scale is of general interest for colliding-beam particle physics experiments at storage rings. It allows one to determine the absolute cross-section value of reaction processes and to quantify the performance of the machine. For instance, at the CERN Large Hadron Collider (LHC) [1], which has started physics operation in 2009, the LHC experiments [2, 3, 4, 5] can use precise cross-section measurements to constrain models of  $pp$  interactions and to detect or quantify new phenomena due to physics beyond the Standard Model of particle physics. In some cases, the required accuracy on the absolute value of the cross section lies in the range 1-5% [6].

In the early phase (April-May) of the LHC 2010 run, a series of experiments were carried out to perform a first luminosity calibration measurement at each Interaction Point (IP). The beam energy was 3.5 TeV (total energy of  $\sqrt{s} = 7$  TeV in the zero-momentum frame of the interacting protons). The optics used were those with  $\beta^* = 2$  m at every IP, corresponding to an individual beam size of about  $45 \mu\text{m}$  (assuming nominal normalized transverse emittance  $\epsilon = 3.75 \mu\text{m}$ ). No external crossing angle was applied, which resulted in a zero net crossing angle at IP1 and IP5. However, due to the presence of a spectrometer dipole, a net crossing angle of  $280$  ( $540$ )  $\mu\text{rad}$  in the vertical (horizontal) plane was present at IP2 (IP8).

Two methods were employed in these first luminosity calibration measurements: the “van der Meer scan” method and the “beam-gas imaging” method [7]. The van der Meer scan method was originally proposed for the Intersecting Storage Rings at CERN [8] and later applied to other colliders, e.g. HERA [9] and RHIC [10]. For a discussion on the application of this method to the LHC, see [11]. The beam-gas imaging method was used for the first time at the LHC [12]. Both methods require a measurement of the individual populations of the bunches contributing to the luminosity. Preliminary results were presented in several places [13]. The data analysis indicates that the dominating contribution to the final uncertainty of the absolute luminosity calibration originates from the bunch current normalization. The purpose of this note is to report on the bunch current normalization during the above experiments and to mention possible improvements for the next series of measurements.

In a first preliminary analysis of the LHC Beam Current Transformer’s (BCT) data, shortly after the luminosity calibration experiments, a conservative estimate of the current normalization was made, which was quoted in various early publications by some of the LHC experiments. In this paper, we report on the results of a more recent work on the bunch population measurement uncertainties. The results of the preliminary analysis are also described and compared to the new results.

The rest of this note is organized as follows. In section 2 an outline of the two beam-overlap measuring methods and of the details of the luminosity calibration experiments are given. Section 3 gives a brief description of the BCT systems. The analysis and results of the bunch population measurements are reported in section 4. Section 5 concludes this work with a discussion and summary.

# 2 Description of the luminosity calibration measurements

The luminosity  $L$  for two counter-rotating bunches (here, 1 stands for Beam1 and 2 for Beam2) with time- and position-dependent density functions  $\rho_1(\mathbf{x}, t)$  and  $\rho_2(\mathbf{x}, t)$  is given by

$$L = f N_1 N_2 \sqrt{(\mathbf{v}_1 - \mathbf{v}_2)^2 - \frac{(\mathbf{v}_1 \times \mathbf{v}_2)^2}{c^2}} \int \rho_1(\mathbf{x}, t) \rho_2(\mathbf{x}, t) d^3x dt \quad (1)$$

for the case where the particles in each bunch are all moving with the same velocity  $\mathbf{v}_1$  resp.  $\mathbf{v}_2$  in the laboratory reference frame (detailed formulas can be found in the literature [14]). Here, we have defined  $f$  the revolution frequency and  $N_1$  resp.  $N_2$  the bunch populations (total number of protons in the bunches that contribute to the luminosity). The bunch particle densities  $\rho_1(\mathbf{x}, t)$  and  $\rho_2(\mathbf{x}, t)$  are normalized such that their individual integrals over full space are unity. The van der Meer and beam-gas imaging methods allow the beam-overlap integral to be measured. Therefore, for determining the luminosity, it is crucial to obtain separately a measurement of the bunch population product  $N_1 N_2$ .

In the van der Meer method, the beams are displaced laterally, along the two transverse axes, and an arbitrary reaction rate is measured as a function of these displacements. Integrating the rates over the displacements

allows one to determine the overlap integral. In the beam-gas imaging method, the beams are left untouched and one uses the fact that high-energy protons will occasionally collide with nuclei of the residual gas and produce tracks within the acceptance of the vertex detector. Reconstructing such distinctive vertices allows one to obtain an image of the transverse bunch profile along the bunch trajectory. From the two individual beam profiles it is then possible to reconstruct the beam-overlap integral [7, 12].

Van der Meer scans, April-May 2010						
LHC fill	Approx. start date time		Approx. stop date time		IP scanned	Bunch pattern
1058	April 24	11:00	April 24	12:30	IP5	3-bunch
1059	April 26	02:30	April 26	06:00	IP8, IP1	2-bunch
1089	May 8	23:00	May 9	03:30	IP5, IP1	2-bunch
1090	May 10	05:00	May 10	07:00	IP2	2-bunch

Table 1: Summary of the April-May 2010 LHC luminosity calibration experiments with the van der Meer method. The bunch patterns are described in the text.

The approximate start and stop times of the six calibration experiments with van der Meer scans are given in table 1. The bunch patterns used during these experiments were either with 3 bunches per beam or with 2 bunches per beam. More exactly, for fill 1058 a 3-bunch pattern was used with RF buckets\* {1, 8941, 17851} of Beam1 and {1, 8911, 17851} of Beam2 nominally filled. For fills 1059, 1089 and 1090 a 2-bunch pattern was used with RF buckets {1, 17851} of Beam1 and {1, 8911} of Beam2 nominally filled. The collision patterns are summarized in table 2.

Fill 1058 3-bunch pattern					Fills 1059, 1089 and 1090 2-bunch pattern				
Beam1 RF bucket	Colliding Beam2 RF bucket				Beam1 RF bucket	Colliding Beam2 RF bucket			
	IP1	IP2	IP5	IP8		IP1	IP2	IP5	IP8
1	1	8911	1	-	1	1	8911	1	-
8941	(8911)	17851	(8911)	1	17851	-	-	-	8911
17851	17851	-	17851	8911					

Table 2: List of bunch crossings in the four insertion regions for the 3-bunch and 2-bunch patterns. In each line the RF bucket of the encountered Beam2 bunch is given for each IP and for the corresponding bucket of the Beam1 bunch. The numbers in brackets indicate a longitudinally displaced crossing, at 11.23 m (anticlockwise) from the actual IP.

The beam-gas method was applied by LHCb over several LHC fills. The analysis concentrated on those for which the beam current uncertainties are smallest (fills 1090, 1101, 1104, 1117, 1118 and 1122) [12].

### 3 Description of the BCT systems

The intensity measurement for the LHC ring is provided by eight current transformers [15]. There are two DC current transformers (DCCT) and two fast beam current transformers (FBCT) installed on the vacuum chamber of each circulating beam. The DCCTs give a measurement of the total current circulating in each ring, irrespective of the time structure of the beams. The FBCTs give a measurement of the bunch populations in each of the 3564 nominal (25 ns) slots of each beam.

For both types of BCT, the architecture is organized in two identical systems, A and B, each one including one BCT per ring. The system A is usually declared online (i.e. operational) by the LHC Beam Instrumentation experts while the system B, declared offline, is kept for the time being as spare or development system. The BCT data discussed in this report originated from the systems A only for the FBCT, while both systems A and B were used for the DCCT.

\*The LHC contains 35640 RF buckets spaced by about 2.5 ns, conventionally numbered from 1 to 35640 and here phased such that bucket 1 of both beams collided in IP1 and IP5.

### 3.1 The DCCT system

The DCCTs, based on the fluxgate magnetometer principle [16], measure the mean current of the circulating beam. The DCCTs for LHC were designed according to tight engineering specifications [17] and built at CERN.

Four measurement ranges are provided in parallel by the front-end electronics and are transmitted to the back-end for analogue filtering and acquisition. The measurements of one selected range are transferred to the LHC Measurement and Logging databases with a frequency of 1 Hz. The four measurement ranges are given in table 3, characterized by their scaling factor, full scale value and least-significant ADC bit (LSB). The range used in the April-May 2010 measurement period was Range 4.

Range	Scaling Factor (elementary charges/V)	Full Scale (elementary charges)	LSB equivalent (elementary charges)
1	1.0E+14	5.0E+14	2.44E+11
2	1.0E+13	5.0E+13	2.44E+10
3	1.0E+12	5.0E+12	2.44E+09
4	1.0E+11	5.0E+11	2.44E+08

Table 3: Specified DCCT ranges. The range used in the April-May 2010 measurement period was Range 4.

The DCCTs are precisely calibrated during each technical stop (at four- to six-week interval) using an external accurate current generator and a method based on the measurement of two known points. The first point is the offset, i.e. the DCCT reading in absence of beam and calibration current. The second point is the DCCT reading when a known current  $I_{\text{cal}}$  is sent in absence of beam into the calibration winding ( $n = 4$  turns). It defines the scaling factor for the range chosen. The value of this second point corresponds to 80% of full scale for the range being calibrated.

The instrument front-end software then allows regular quick calibration checks to be performed based on a less precise integrated current generator. The calibration sequence for all four ranges takes 3.6 seconds. A time too short to perform a precise calibration, but long enough to verify that the overall system does not degrade and stays within predefined tolerances ( $\sim 10\%$ ) with respect to the predicted calibration factors. The offset variations for Range 4 were logged during the periods with no beam and are the subject of section 4.

A more detailed description of the DCCT system is given elsewhere [15, 16, 17, 18].

### 3.2 The FBCT system

The FBCT measurement system is composed of the measurement device [19], front-end electronics, an acquisition system [20], and a software control system. The system was designed to comply with the measurement specification [17]. The beam current is measured using a 1:40 toroid transformer from Bergoz Instrumentation. The signal is split in an RF distributor into two dynamic ranges, each of them providing measurements in two bandwidths: 200 MHz for bunch by bunch measurements and about 2 MHz for turn-based measurements. The four measurement signals are independently integrated using the LHCb2002 analog integrator ASIC and sampled using 14 bit ADCs clocked synchronously with the beam. The entire measurement process is driven in the hardware by two Digital Acquisition Boards (DABs) [21]. Each DAB processes two integrated signals of the same bandwidth using an FPGA. The measured data are stored either in the FPGA on-chip memory, or in the external synchronous SRAM for large-volume measurements. The real-time software running in the front-end controller (FEC) provides the necessary system control, calibration procedure (each integrator has its own offset and scaling factor), conversion of the stored measurements to the number of charges, and data publishing. Four measurement modes are provided:

- Capture: a snapshot of the intensity measurement in each bunch slot on the high bandwidth channel for a specified number of turns triggered by an LHC machine event on request.
- Turn Sum: turn by turn total intensity (summing over all 3564 bunch measurement slots, on the high bandwidth channel) mainly used for online fixed displays and dedicated measurements for machine developments,

- Slot Sum: 3564 bunch slot intensities on the high bandwidth channel each averaged over a specified number of turns,
- Sum Sum: a measurement of Turn Sum over a specified number of turns (usually 225 turns to give one value every 20 ms) from the low bandwidth channel used for fixed displays and lifetime calculation.

The data analyzed in this work are from the Slot Sum mode with a specified number of 900 samplings for averaging (taken in 3600 turns with one sampling every fourth turn).

Each FBCT system is calibrated by 5  $\mu$ s long current pulses of specific amplitudes. The calibration pulses are generated in a calibrator, implemented into a VME64x 6U board, and they are transported to the calibration circuit installed in the measurement device using 7/8" Heliflex cables. However, in the early commissioning phase of the LHC, the current normalization of the FBCT was not performing as expected and their calibration was still relying on the DCCT, by comparing the sum over slots with the total current, as discussed below.

A more detailed description of the FBCT system is given elsewhere [15, 19, 20, 21, 22].

## 4 Bunch population data analysis

In the April-May 2010 measurements, the individual bunch populations  $N_i$  (of each beam) were obtained assuming that the sum of populations of all nominally filled bunches  $i = 1, \dots, n$  ( $n = 2$  or  $3$ , depending on the fill), as measured by the FBCT, was equal to the value of the total beam population obtained from the DCCT  $N_{\text{tot}}$ , after subtracting a possible amount of “ghost” charge  $N_{\text{ghost}}$ . The ghost charge is here defined as the charge not visible to the FBCT, i.e. the summed charge of all those 25 ns slots for which the slot charge is below the FBCT threshold. The total intensity was taken from  $N_{\text{tot}} = \alpha \cdot S_{\text{DCCT}}$ , where  $\alpha$  is the absolute scale factor of the DCCT (elementary charges/V) and  $S_{\text{DCCT}}$  the signal measured by the DCCT (V) after correcting for a baseline offset. The amount of ghost charge was estimated from detector data by the experiments and resulted to be relatively small compared to the total uncertainty on the bunch currents (see detailed analysis in section 4.3). A common scale factor to transform FBCT signals into bunch populations can be defined as

$$a = \frac{N_{\text{tot}} - N_{\text{ghost}}}{\sum_{i=1}^n S_i} . \quad (2)$$

The sum runs over all nominally filled slots ( $i = 1, \dots, n$ ). Here, the  $S_i$  values are the FBCT values corrected for spill-over, as explained in see section 4.2. Then, the bunch populations are

$$N_i = a S_i . \quad (3)$$

The uncertainties on the bunch populations may arise from the total population  $N_{\text{tot}}$ , the individual bunch signals (i.e. FBCT signals  $S_i$ ) or the ghost charge  $N_{\text{ghost}}$ . We address these separately in order of decreasing importance for the April-May 2010 measurements, namely, first the total population uncertainties, then the FBCT signals and finally the ghost charge.

### 4.1 Total beam population

Because the absolute scale of the bunch charges measured by the FBCT is renormalized to that of the total circulating beam current reported by the DCCT, the uncertainty on the absolute bunch intensity is dominated by that on the overall accuracy of the DCCT. The DCCT readings may be distorted by various effects [18] such as temperature drifts, electromagnetic pick-up in cables, mechanical vibrations of the transformer assembly, etc. For the beam intensities and with the sparse bunch pattern used in the April-May 2010 van der Meer scans, the dominant uncertainty is associated with the absolute scale accuracy of the DCCT and its baseline drifts (a known issue for this type of instrument). The baseline drifts are analyzed in detail in section 4.1.1 below. The absolute scale accuracy of the DCCT is briefly discussed in section 4.1.2.



#### 4.1.1 DCCT baseline subtraction

The baseline offsets were measured with no beam in the LHC, before injection and then again after dumping the beam. These data were analyzed to extract an estimated offset during the presence of beam. The treatment of the baseline offset in the preliminary analysis is described first. Then, the detailed analysis results are presented.

##### 4.1.1.1 Preliminary analysis

As will be detailed in section 4.1.1.2 below, the time history of the DCCT baselines reveals fluctuations on a wide range of time scales. An early estimate of these fluctuations suggested that with the automated averaging algorithm applied to the DCCT data at that time, the DCCT baselines measured before and after each fill were each affected by an equivalent peak-to-peak (or “envelope”) uncertainty of  $\pm 1 \cdot 10^9$  protons in total beam intensity. This was conservatively translated into a peak-to-peak uncertainty of  $\pm 2 \cdot 10^9$  protons on the total beam current reported by the DCCT in the period between the two baseline measurements bracketing the fill under study. This led to the following estimate of the uncertainty on the measured bunch intensity  $N_i$  associated with the DCCT baseline subtraction:

$$\frac{\Delta N_i}{N_i} = \frac{\pm 2 \cdot 10^9}{n \cdot \langle N_i \rangle} = \frac{\pm 2 \cdot 10^9}{N_{\text{tot}}} \quad (4)$$

where  $\Delta N_i$  is the peak-to-peak uncertainty on  $N_i$ ,  $n$  is the total number of bunches per beam, and  $\langle N_i \rangle$  is the mean charge per bunch. It should be stressed that  $\Delta N_i$  is a peak-to-peak or “tolerance” uncertainty, in the sense that it is meant to cover the full possible range of measurement errors; in other words, the true value of  $N_i$  may lie anywhere in the interval  $N_i \pm \Delta N_i$ , but not outside. Interpreting  $\Delta N_i$  as a standard deviation would therefore be an overestimate. Under the assumption of a uniform distribution of half width  $\Delta N_i/N_i$ , the fractional standard deviation uncertainty associated with DCCT baseline drifts was estimated by

$$\frac{\sigma_{N_i}}{N_i} = \frac{\Delta N_i}{N_i} \cdot \frac{1}{\sqrt{3}} = \frac{1.15 \cdot 10^9}{n \cdot \langle N_i \rangle} = \frac{1.15 \cdot 10^9}{N_{\text{tot}}} \quad (5)$$

This led, for example, to a bunch-charge uncertainty (for each beam) of  $\sigma_{N_i}/N_i = 5.8\%$  in the case of a beam with two circulating bunches containing  $1 \cdot 10^{10}$  protons each.

Under the conditions of the April-May 2010 scans considered in this preliminary analysis, the DCCT baseline corrections dominated the bunch-charge uncertainties. The estimated impact, on the luminosity scale, of the two single-beam current uncertainties, as well as their combination with the DCCT scale uncertainty will be discussed in section 5.

##### 4.1.1.2 Detailed Analysis

In view of the magnitude of the DCCT baseline uncertainties, a more precise quantitative characterization of these errors and of their degree of correlation between the two beams was required. Figure 1 shows the DCCT (system A) data as retrieved from the LHC logging database (logging frequency of 1 Hz). The same graphs for system B can be found in the appendix. Unless otherwise specified, all other figures with DCCT data are for system A. The RMS of the DCCT measurement data (1 Hz) amounted to about  $\sigma_0 = 0.9 \cdot 10^9$  protons for Beam1 and  $0.7 \cdot 10^9$  protons for Beam2. To study the offset variations the DCCT measurements were averaged over a given time bin to suppress fast fluctuations. Assuming a Gaussian noise, the RMS  $\sigma_m$  should decrease inversely proportional to the square root of the number of measurements used in the averaging:  $\sigma_m = \sigma_0/\sqrt{m}$ , where  $m$  is the number of data points in the chosen time bin.

Figure 2 shows the RMS as a function of the size of the averaging time bin for a period without beam on 26/27 April 2010 (a plot for a second period is shown in the appendix). The RMS deviates from the behaviour expected for pure single-Gaussian noise, indicating the presence of fluctuations with different time scales. In the absence of understanding of the slow variations, the uncertainties are quoted here in terms of peak-to-peak bounds  $\pm \Delta N_{\text{tot}}$ , defined as half the distance between the smallest and the largest value obtained with the given time bin averaging. Based on figure 2, a size of 300 s for the averaging time window was chosen, such that the RMS was no longer dominated by the fast fluctuations and the chosen time bin was still short compared to the duration of a van der Meer scan (which was one to two hours). For

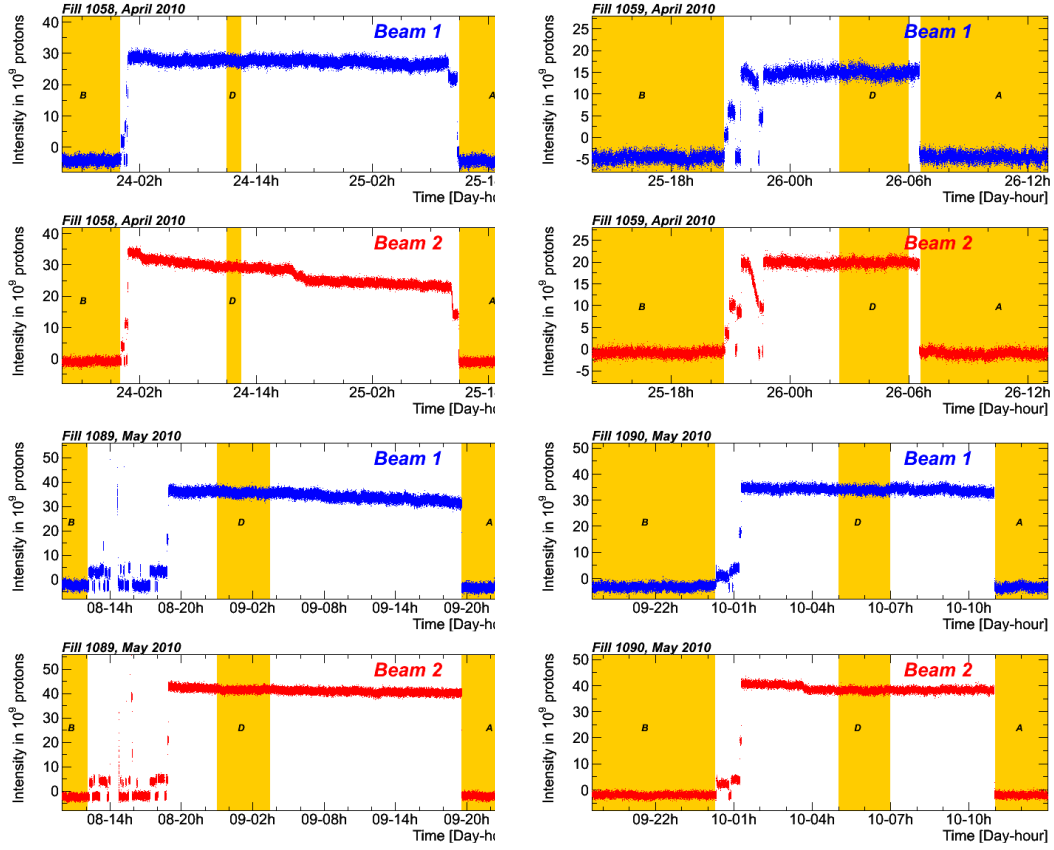


Figure 1: DCCT system A data for the van der Meer scan fills, as retrieved from the LHC logging database. The periods “before”, “during” and “after” the scans used to determine the beam currents are indicated by the shaded bands B, D and A.

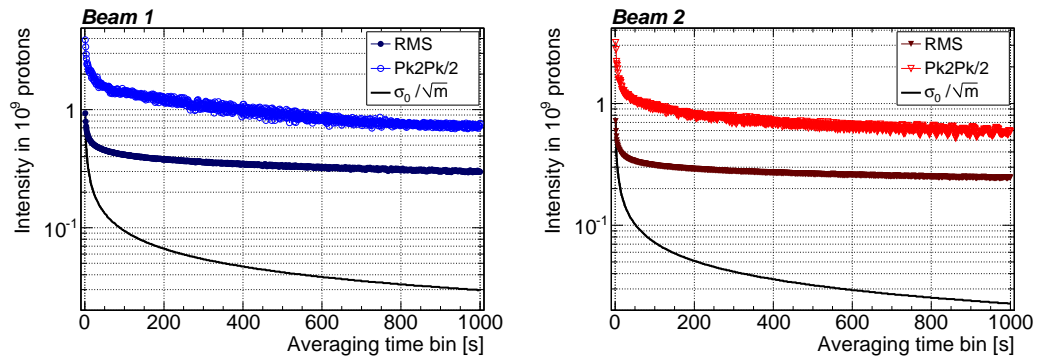


Figure 2: Background period without beam for 26/27 April 2010 for Beam1 (left) and Beam2 (right). The RMS (solid symbols) and the peak-to-peak bound (empty symbols) are plotted versus the size of the averaging time bin. The black curve is the expectation for a single-Gaussian noise, normalized to the value at the smallest time bin size.



larger time bin size, the peak-to-peak bound becomes almost insensitive to the time bin size (a change by about 25% from 300 s to 1000 s).

The offset to be subtracted from the DCCT intensity measurements during a van der Meer scan was extracted from a linear interpolation of the offsets measured in the periods “before” and “after” the relevant LHC fills. A zoom on these periods is shown in figure 3 for fill 1059 (see figures in the Appendix for the other fills). The interpolated offset was subtracted from the DCCT measurement result “during” the van der Meer scan. The offset uncertainty was taken to be the largest of the two peak-to-peak bounds (before and after the fill).

The central values of the DCCT measurements before, during and after the scans depend on the choice of the evaluation windows “B”, “D” and “A” of figure 1. The values obtained for the peak-to-peak bounds depend on the choice of the evaluation windows before and after the fills, as well as on the choice of the averaging time bin size (as discussed above). The evaluation windows were chosen (within the constraints of available data with no beam) to be of a length somewhere between the duration of a van der Meer scan period and the length of a fill, i.e. in the order of a few hours. They were placed as close as possible to the start and end of the fill.

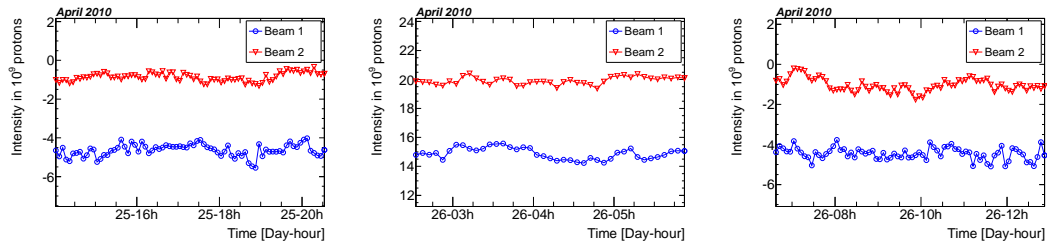


Figure 3: The measured intensity versus time in periods before (left), during (middle) and after (right) a van der Meer scan (fill 1059) for Beam1 (blue circles) and for Beam2 (red triangles), with 300 s averaging time.

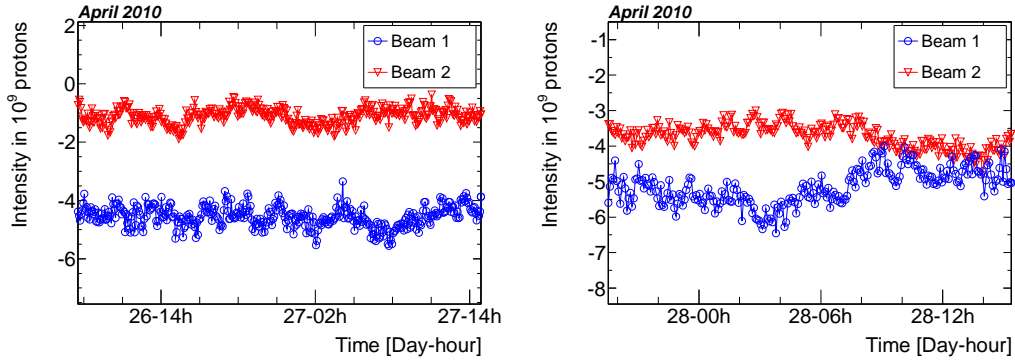


Figure 4: Two periods without beam: April 26/27 (left) and April 27/28 (right), 2010. The DCCT signal is shown versus time for Beam1 (blue circles) and Beam2 (red triangles), with 300 s averaging time.

This method of estimating the offset was tested on a data sample taken during two no-beam periods of 30 hours and 20 hours from April 26 to 28. Figure 4 shows the evolution of the offset of the DCCT intensity measurements during these two periods. The length of the evaluation windows “before” and “after” was two hours, similar to the length of the measurement periods available for the van der Meer scan fills. The gap between the periods “before” and “after” the test period was varied from 1.5 hour to the maximum possible (25 and 15 hours, depending on the chosen no-beam period). The measured value was averaged over 1.5 hour at the centre between the “before” and “after” windows. Figure 5 shows the result of the test. The offset estimated using the above interpolation method is compared to the actual (measured) offset as a function of the gap length. The two values are consistent.

The results for the averaged intensity before, during and after each van der Meer scan are summarized in table 4 for system A and table 5 for system B. The measurement uncertainties are peak-to-peak bounds

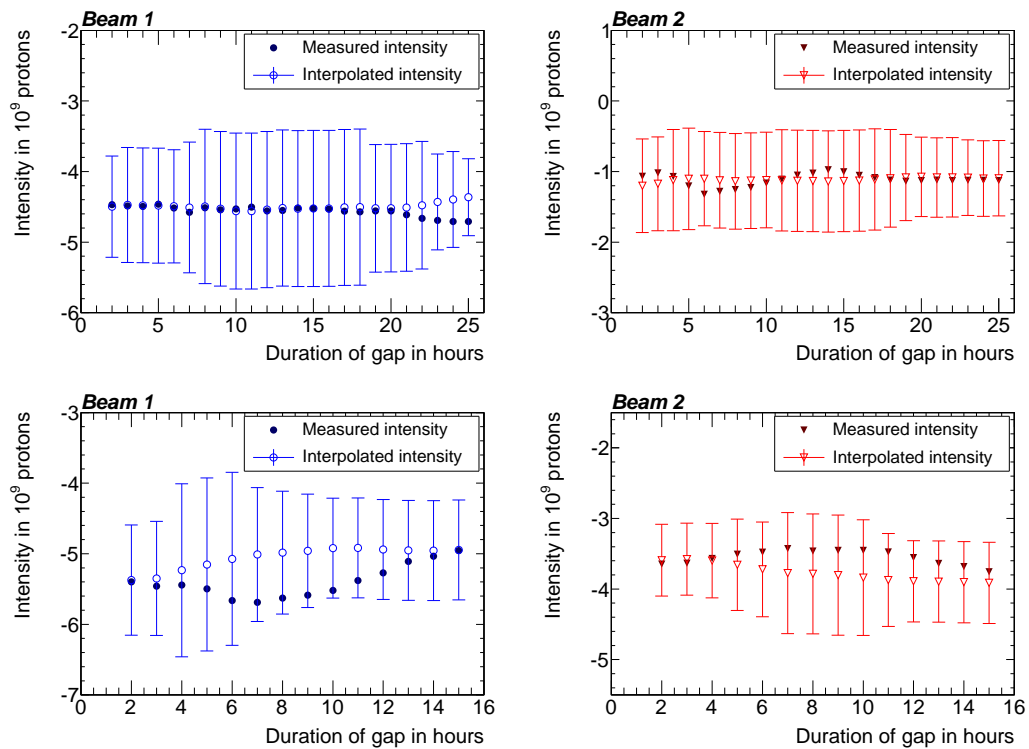


Figure 5: Comparison of the measured intensity average with the interpolated value during the two periods without beam for 26/27 (top) and 27/28 (bottom) April 2010 for Beam1 (left) and Beam2 (right). The solid symbols correspond to the intensity average measured during the gap and the empty symbols to the value from interpolation across the gap. The error of the interpolated intensity average is given by the largest of the peak-to-peak bounds found before and after the gap.

$\pm\Delta N_{\text{tot}}$ , as defined above. The last column shows the intensities, averaged in the periods covering the van der Meer scan (as defined in table 1) and with the baseline subtracted as described in this section. The DCCT measurements of the beam intensities exhibited no significant decay during the van der Meer scans. The (more sensitive) FBCT signals showed a relative drop ranging from 0.1% to 1.6%, depending on the bunch and fill number (see figure 8 in section 4.2).

Fill nr.	LHC ring $j$	System A DCCT intensity $\alpha S_{\text{DCCT}} \cdot 10^{-9}$			LHC intensity $N_{\text{tot},j} \cdot 10^{-9}$ baseline-corrected
		Before	During	After	
1058	1	$-4.3 \pm 0.8$	$27.7 \pm 0.5$	$-4.5 \pm 0.7$	$32.1 \pm 0.8$
	2	$-0.8 \pm 0.6$	$29.4 \pm 0.4$	$-1.0 \pm 0.4$	$30.3 \pm 0.6$
1059	1	$-4.6 \pm 0.8$	$14.9 \pm 0.7$	$-4.5 \pm 0.7$	$19.4 \pm 0.8$
	2	$-0.9 \pm 0.5$	$19.9 \pm 0.5$	$-1.0 \pm 0.6$	$20.9 \pm 0.6$
1089	1	$-2.3 \pm 0.8$	$35.6 \pm 0.8$	$-3.2 \pm 0.7$	$38.3 \pm 0.8$
	2	$-2.4 \pm 0.5$	$41.5 \pm 0.5$	$-2.0 \pm 0.5$	$43.7 \pm 0.5$
1090	1	$-3.2 \pm 0.7$	$33.9 \pm 0.6$	$-3.4 \pm 0.8$	$37.2 \pm 0.8$
	2	$-2.0 \pm 0.5$	$38.2 \pm 0.5$	$-2.0 \pm 0.3$	$40.2 \pm 0.5$

Table 4: DCCT System A total population measurements for all April-May 2010 fills with van der Meer scans. The uncertainties quoted here for beam  $j$  are peak-to-peak bounds  $\pm\Delta N_{\text{tot},j}$  as defined in the text.

Fill nr.	LHC ring $j$	System B DCCT intensity $\alpha S_{\text{DCCT}} \cdot 10^{-9}$			LHC intensity $N_{\text{tot},j} \cdot 10^{-9}$ baseline-corrected
		Before	During	After	
1058	1	$-3.2 \pm 0.6$	$29.3 \pm 0.2$	$-2.8 \pm 0.5$	$32.4 \pm 0.6$
	2	$-4.8 \pm 0.7$	$25.3 \pm 0.5$	$-5.3 \pm 0.6$	$30.3 \pm 0.7$
1059	1	$-2.9 \pm 0.6$	$15.6 \pm 0.7$	$-3.6 \pm 0.6$	$19.0 \pm 0.6$
	2	$-5.3 \pm 0.5$	$15.4 \pm 0.6$	$-4.9 \pm 0.7$	$20.4 \pm 0.7$
1089	1	$-2.2 \pm 0.5$	$36.2 \pm 0.6$	$-2.3 \pm 0.4$	$38.4 \pm 0.5$
	2	$+0.4 \pm 0.4$	$43.6 \pm 0.6$	$+0.1 \pm 0.7$	$43.3 \pm 0.7$
1090	1	$-2.3 \pm 0.4$	$35.1 \pm 0.6$	$-2.4 \pm 0.4$	$37.5 \pm 0.4$
	2	$+0.1 \pm 0.7$	$40.8 \pm 0.4$	$-0.5 \pm 0.5$	$41.0 \pm 0.7$

Table 5: DCCT System B total population measurements for all April-May 2010 fills with van der Meer scans. The uncertainties quoted here for beam  $j$  are peak-to-peak bounds  $\pm\Delta N_{\text{tot},j}$  as defined in the text.

The two DCCT systems, A and B, give consistent results and similar peak-to-peak bounds. However, because the slow fluctuations of the measurements are presently not well understood, the data of system A and B were combined (for each fill and beam) using an unweighted average. Conservatively, a fixed peak-to-peak bound of  $\pm 0.8 \cdot 10^9$  was assigned to all resulting intensity values. This value corresponds to the largest peak-to-peak bound from the individual measurements. The results for the averaged intensity for each van der Meer scan are summarized in table 6. In the last column, the results of the preliminary analysis mentioned in section 4.1.1.1 are shown for comparison.

To quantify the correlation between the fluctuations of the two beam current measurements, Beam1 DCCT data were plotted against Beam2 DCCT data. The resulting scatter plots were fitted with a bivariate Gaussian parametrization:

$$f(x,y) = \frac{1}{2\pi\sigma_x\sigma_y\sqrt{1-\rho^2}} \cdot e^{-\frac{1}{2(1-\rho^2)}\left[\frac{(x-\mu_x)^2}{\sigma_x^2} + \frac{(y-\mu_y)^2}{\sigma_y^2} - \frac{2\rho(x-\mu_x)(y-\mu_y)}{\sigma_x\sigma_y}\right]}. \quad (6)$$

In case of no correlation, one expects  $\rho = 0$ .

Figure 6 shows the correlation for the differences between two successive (300 s averaged) measurements for all available April-May DCCT data. Note that these data include periods without and with beams. Therefore, a correlation due to the beam current decay should (if anything) enhance the correlation in this figure. The result of the bivariate Gaussian fit gives here  $\rho = 0.017 \pm 0.172$ , indicating that correlations in fast variations (on the time scale of 300 s) are negligible.

Fill nr.	LHC ring $j$	Detailed analysis (this work) LHC intensity, systems A and B $N_{\text{tot},j} \cdot 10^{-9}$ baseline-corrected	Preliminary analysis LHC intensity, system A $N_{\text{tot},j} \cdot 10^{-9}$ baseline-corrected
1058	1	$32.3 \pm 0.8$	$31.8 \pm 2.0$
	2	$30.3 \pm 0.8$	$28.4 \pm 2.0$
1059	1	$19.2 \pm 0.8$	$18.9 \pm 2.0$
	2	$20.7 \pm 0.8$	$20.6 \pm 2.0$
1089	1	$38.4 \pm 0.8$	$38.1 \pm 2.0$
	2	$43.5 \pm 0.8$	$43.7 \pm 2.0$
1090	1	$37.4 \pm 0.8$	$37.4 \pm 2.0$
	2	$40.6 \pm 0.8$	$40.0 \pm 2.0$

Table 6: DCCT total population measurements for all April-May 2010 fills with van der Meer scans. The uncertainties quoted here for beam  $j$  are peak-to-peak bounds  $\pm \Delta N_{\text{tot},j}$  as defined in the text.

Figures 7(a), 7(b) and 7(c) show the correlation between the current measurements of Beam1 and Beam2 for all studied periods “before” and “after” van der Meer scans, and for the no-beam periods defined above. The data taken “before” and “after” van der Meer scans, and for one of the two no-beam periods, indicate a negligible correlation between the two beams ( $\rho = -0.013 \pm 0.150$  and  $0.003 \pm 0.165$  respectively). The rightmost graph (the second no-beam period) shows an anti-correlation between the two beams ( $\rho = -0.632 \pm 0.129$ ). This is interpreted as a fortuitous effect from a slow drift of the baseline, already visible in figure 4(b).

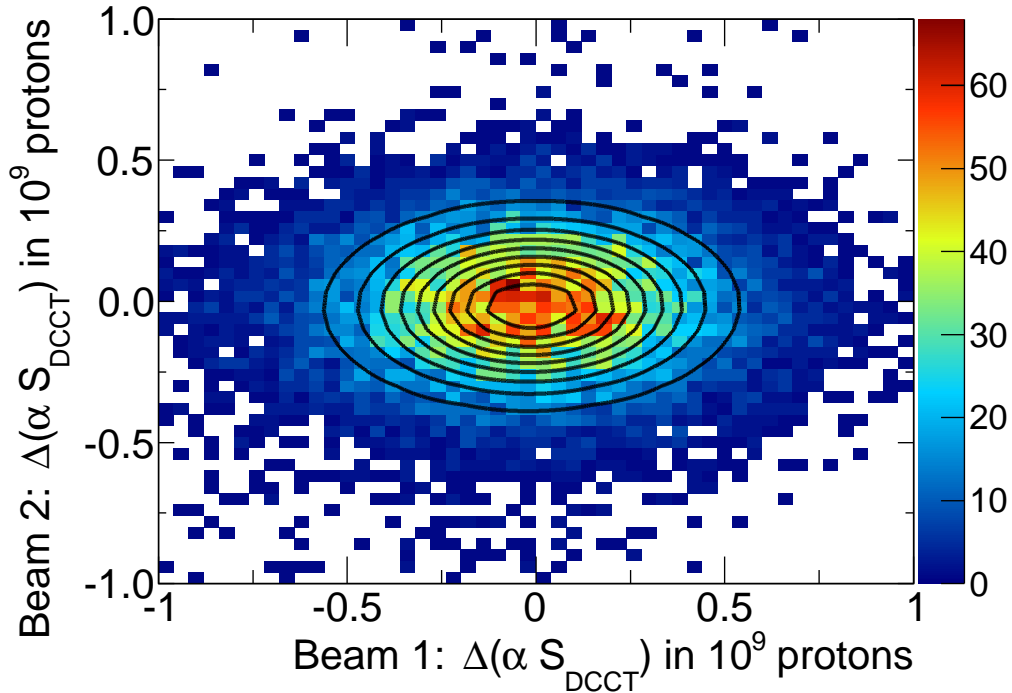


Figure 6: Correlation between Beam1 and Beam2 DCCT difference measurements (with 300 s averaging) for all data taken in April-May 2010. The black lines represent the fitted two-dimensional Gaussian.

#### 4.1.2 Absolute scale of the DCCT

The uncertainty on the scaling factor  $\alpha$  defined in section 4 has at least four possible sources:

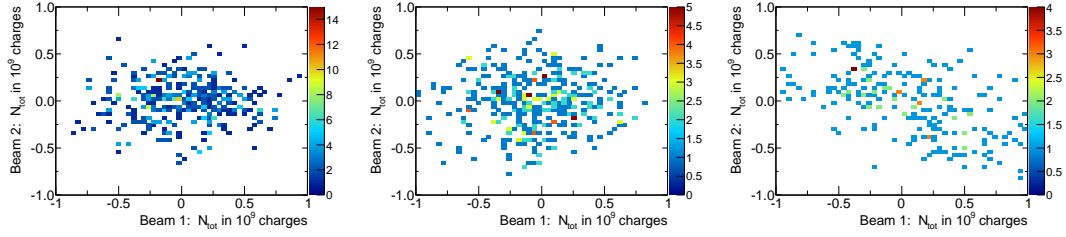


Figure 7: Correlation between Beam1 and Beam2 current measurements. On the leftmost graph, data are plotted from periods “before” and “after” van der Meer scans defined in figure 3. On the middle (rightmost) graph, data are plotted for the first (second) no-beam period defined in figure 4.

- inaccuracy of the commercial current generator used for calibration,
- misbehaviour of the DCCT linked to the LHC filling pattern,
- non-linearity of the measurement system between the working point (measurement) and the calibration points,
- long term evolution (between calibration periods and van der Meer scan periods).

The accuracy and linearity of the current source quoted by the manufacturer is below 0.1%. Although not independently verified, this potential source of uncertainty is believed to be negligible for the current work. A systematic study of the accuracy and linearity of the current source is under way.

Concerning the second item, a faulty behaviour was observed with bunch trains of 150 ns and 50 ns spacing in the LHC. The cause of this behaviour was recently traced back to a saturation effect of amplifiers in the FE boards for specific bunch patterns. The effect was reproduced in the laboratory. However, such misbehaviour was not observed for the patterns used in the April-May van der Meer scans (with 2 or 3 isolated bunches), neither with beam nor in the laboratory. Furthermore, during the early phase of LHC commissioning, a number of asynchronous dump tests were performed during which the RF voltage of the accelerating cavities was abruptly switched off. In these events, the current measured by the DCCT showed no change on the time scale of the debunching process, indicating that, with few isolated bunches (as in the case of the April-May 2010 van der Meer scan filling patterns), the DCCT was not sensitive to the bunch length in the range of interest.

At the present level of understanding, the main source of uncertainty is believed to be the stability over time. Based on precise calibration points taken during technical stops and on the analysis of the regular calibration checks, the absolute scale accuracy is currently estimated to be  $\Delta\alpha/\alpha \approx \pm 2\%$  for each ring, again quoted here as a peak-to-peak bound. This value was used for both preliminary and detailed analyses. Because this uncertainty appears dominated by variations over time observed in the calibration data, the scale factor uncertainties between the DCCT measurements taken at two different times or taken from two different devices are thought to be partly uncorrelated. However, until a better understanding of these uncertainties is obtained, these should be treated (conservatively) as correlated uncertainties. Detailed studies of the scale factor stability and linearity are ongoing.

## 4.2 Relative bunch populations

The FBCT measures the total charge contained in 25 ns long time slots centered on the nominal 40MHz bunch slots. Small timing errors and imperfections in the transformer response may result in a few percent of the total bunch signal appearing in the time slot adjacent to that of the bunch under consideration. This is an instrumental effect and does not imply that protons themselves diffused into the corresponding RF buckets. The first step of the data reprocessing therefore consists in adding back to the correct time slot, the charge originally reported in the neighbouring one. In practice, the reprocessed FBCT signals are given by  $S_i = S_i^{\text{raw}} + S_{i+1}^{\text{raw}}$  where  $i$  is the slot number of each nominally filled bunches and  $S_i^{\text{raw}}$  indicates the raw FBCT signals. For the April-May 2010 period, this correction typically amounted to a 2-5% effect and had

little impact on the final results, since the sum of bunch populations was normalized to the DCCT total population.

During the initial phase of LHC operation the FBCT data sent to permanent storage were zero-suppressed using a signal threshold of  $1 \cdot 10^7$  elementary charges per slot (fills 1058 and 1059). The threshold was later increased to  $1 \cdot 10^8$  elementary charges (fills 1089 and 1090) to reduce the rate of noise spikes. For the FBCT data analysis, a cut at  $5 \cdot 10^8$  elementary charges is applied.

Figure 8 shows the FBCT signals of the nominally filled bunch slots as a function of time for the four relevant fills and for both beams separately. Each signal was here normalized to its value at the start of the graph in order to make the small relative change of the bunch populations more visible.

A possible non-linearity of the FBCT system was checked and estimated by comparing the FBCT measurements to those of an independent system, namely the ATLAS BPTX system [23], which also provides a measurement of the relative bunch populations. The two ATLAS BPTX stations are composed of electrostatic button pick-up detectors which are arranged each on one side of the experiment at 175 m from IP1 (on the incoming beam pipe). Each bunch induces a bipolar signal whose positive part integral depends linearly on the bunch intensity. The relative bunch populations as seen by the FBCT and ATLAS BPTX are reported in table 7 as a percentage of the summed signals (for each system independently) of the nominally filled bunches. The last column of the table shows the relative bunch populations obtained from the raw (non-corrected) FBCT signals, indicating that the applied corrections changed the population values by less than 0.4% (relative change).

Fill	LHC ring $j$	bunch $i$	RF Bucket	$N_{i,j}^{\text{BPTX}}$ (%)	$N_{i,j}^{\text{FBCT}}$ (%)	$N_{i,j}^{\text{FBCTraw}}$ (%)
1058	1	1	1	28.8	29.6	29.7
		2	8941	37.3	36.2	36.2
		3	17851	33.9	34.2	34.1
	2	1	1	33.7	33.7	33.7
		2	8911	36.0	35.2	35.2
		3	17851	30.3	31.1	31.1
1059	1	1	1	46.5	46.8	46.8
		2	17851	53.5	53.2	53.2
	2	1	1	49.9	50.0	50.0
		2	8911	50.1	50.0	50.0
1089	1	1	1	50.1	50.0	49.9
		2	17851	49.9	50.0	50.1
	2	1	1	51.3	51.1	51.1
		2	8911	48.7	48.9	48.9
1090	1	1	1	54.4	53.5	53.6
		2	17851	45.6	46.5	46.4
	2	1	1	48.1	48.3	48.3
		2	8911	51.9	51.7	51.7

Table 7: Relative bunch population measurements of the FBCT and ATLAS BPTX averaged over the duration of each van der Meer scan period.

The results listed in table 7 show that the measurements of the ATLAS BPTX and the FBCT systems differed by up to  $\pm 3\%$  (relative difference). The statistical uncertainty was negligible ( $< 0.1\%$ ). A closer look reveals that for the larger FBCT relative population in a given fill, the BPTX relative population is systematically smaller, and vice versa for the smaller FBCT relative population. A preliminary study of the data of a later LHC fill (fill 1295, August 2010), with 48 bunches per ring, indicates that the relation

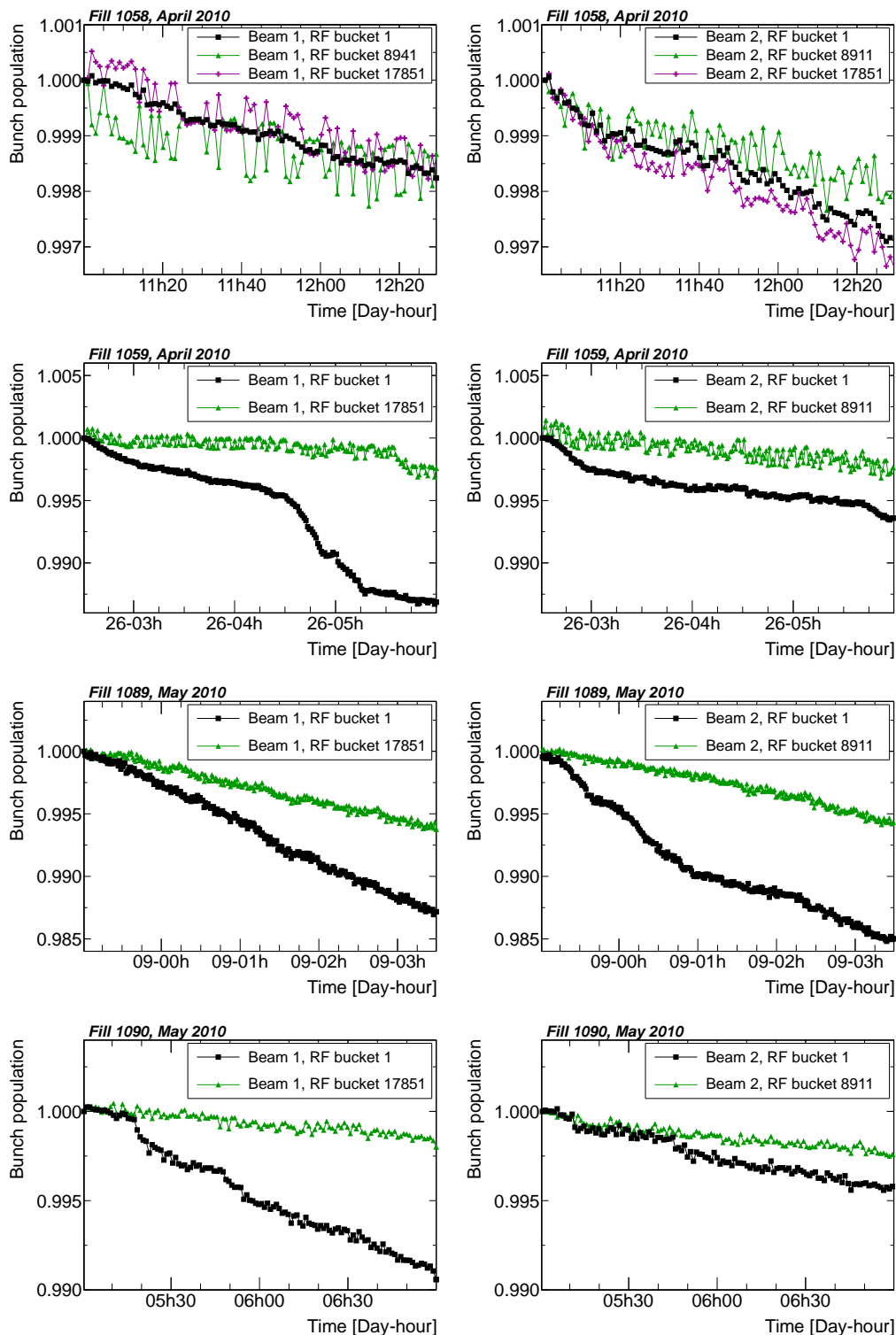


Figure 8: FBCT signals of the nominally filled bunch slots as a function of time for the four van der Meer scan fills. Left: Beam1. Right: Beam2. Each signal is normalized to its first value.



between the FBCT and ATLAS BPTX may suffer from a small offset at zero beam current, which could explain the above observation. This is illustrated in figure 9 where the signal of the ATLAS BPTX is shown versus the FBCT signal for each individual bunch (averaged here over 20 minutes). The data were fitted with a straight line, giving a slope of  $0.8759 \pm 0.00097$  ( $0.9045 \pm 0.00076$ ) for Beam1 (Beam2) and an offset of  $-4.60 \pm 0.08$  ( $-5.48 \pm 0.06$ )  $10^9$  elementary charges. Such an offset could explain why the BPTX relative populations systematically differ from the FBCT values in the manner explained above. The origin of this offset is still under study. Given our present understanding of the FBCT and BPTX, the values of the FBCT system are used for the relative bunch populations and a relative peak-to-peak bound of  $\pm 3\%$  is assigned to these values.

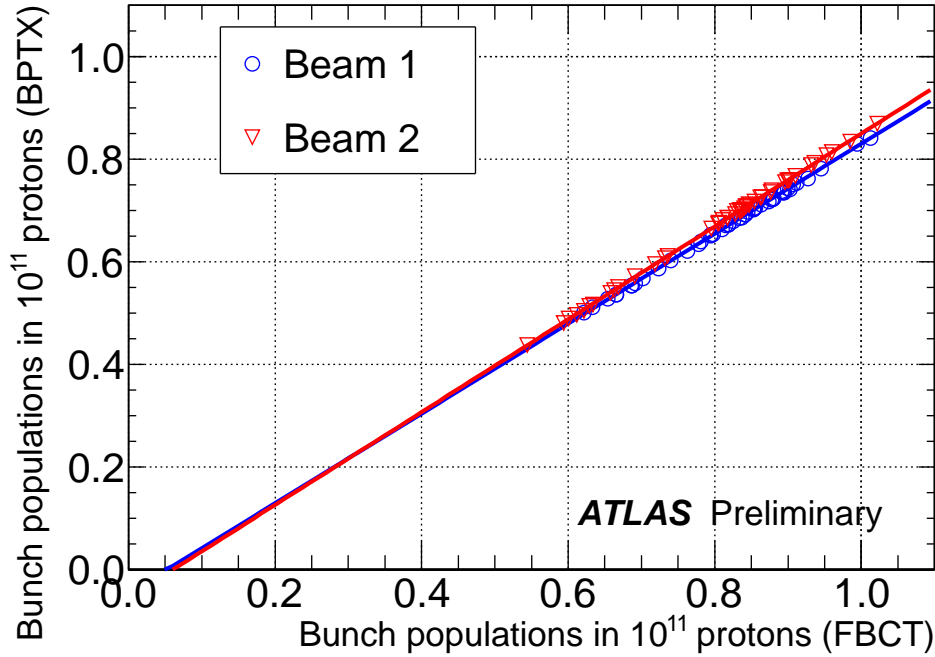


Figure 9: ATLAS BPTX signal versus FBCT signal for LHC fill 1295 (August 2010). Each data point corresponds to a different bunch. The lines are the results of a straight line fit (see text).

### 4.3 Ghost charge and satellite bunches

Currently, the FBCT sum is normalized to the DCCT total current and therefore the difference between the two measurements cannot be used to estimate the amount of charge not contributing to luminosity. In addition, as will be shown here, part of the beam charge may be captured in RF buckets that are within a few ns of the nominally filled bunches, i.e. within the same 25 ns slot. For such satellite bunches, it is not clear how the FBCT signals should be used to extract the luminous and non-luminous charge. This may depend on the specificities of the luminosity monitors used during the van der Meer scans and on the response of the FBCT within the 25 ns slot. For the April-May 2010 measurements, selected data rates from the experiments were used to constrain or measure the ghost charge and satellite bunches. LHCb carried out an analysis of beam-gas interaction data taken with a “low bias” trigger. ATLAS and CMS both performed a study of satellite bunches (in the neighbourhood of the colliding bunches) based on vertex reconstruction of longitudinally displaced interactions. CMS also made an analysis based on precise timing which allowed one to quantify the satellite bunch populations. Both CMS and ATLAS took advantage of the fact that there was no crossing angle at IP1 and IP5, and both relied on the occurrence of  $\sqrt{s} = 7$  TeV p-p interactions (as opposed to beam-gas interactions for the LHCb method). These three different types of analyses are discussed next.

### 4.3.1 Ghost charge from beam-gas interactions

LHCb monitored the beam-gas rates for both beams with a “low bias trigger”. This trigger required a minimum detected activity in at least one direction (left or right from IP8). The left side requirement was a “PU multiplicity” of more than three. The PU multiplicity is the number of hits in one station of the “Pile-Up” system, a silicon detector covering radii from 8 to 42 mm around the beam axis and located at  $-31.5 \leq z \leq -22$  cm. Throughout this work, we use the convention  $z = 0$  at the nominal IP position and  $z > 0$  in the clockwise LHC direction, i.e. in the Beam1 direction. The right side requirement was more than two hits in the SPD (Scintillator Pad Detector [5]) and at least one Hadronic Calorimeter cluster with transverse energy of more than 240 MeV. The rate measured in the bunch-bunch crossings (b-b) were used for luminous region monitoring in the van der Meer scans. The beam-gas rates from bunch-empty (b-e) and empty-bunch (e-b) crossings were used for beam-gas imaging and for normalization of the ghost charge. The rate measured in empty-empty crossings (e-e) were used for measuring ghost charge. The trigger was armed for every 25 ns slot, but blocked for one clock cycle (25 ns) after each trigger. To collect maximum (minimum bias) data in b-b crossings, a trigger was forced at every b-b crossings. As a consequence, practically no data could be collected for the slots just after a b-b crossing. The triggers were also forced (randomly) on 21.4% of the b-e crossings, 14.3% of the e-b crossings and 0.002% of each e-e crossing for fills 1059, 1089 and 1090. For fill 1058, the forced fractions were 42.9%, 28.6% and 0.004%.

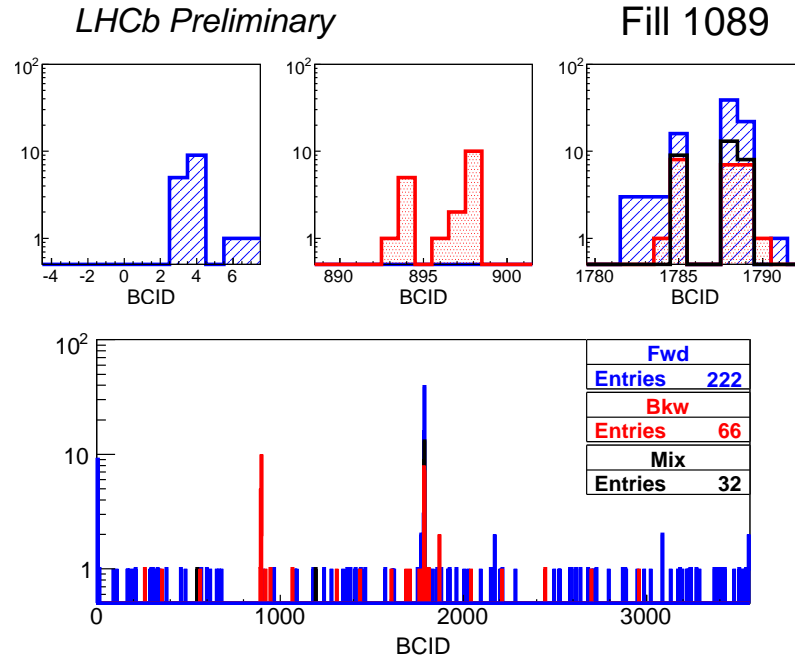


Figure 10: Number of forward (blue, hatched), backward (red, dotted) and mixed (black, empty) events as a function of Bunch Crossing ID for e-e crossings in fill 1089. BCIDs are counted modulo 3564.

The reconstructed interactions of non-b-b crossings were divided in three categories, “forward”, “backward” or “mixed”. A general cut  $|z_{\text{vtx}}| < 2$  m was applied, where  $z_{\text{vtx}}$  was the longitudinal position of the vertex as measured by the VELO (LHCb VERTex LOCator [5]), defined such that  $z_{\text{vtx}} = 0$  was the nominal interaction point, IP8, at LHCb. A vertex was also required to have at least three VELO tracks. A forward event was defined by the requirement that all vertex tracks pointed in the direction of the LHCb dipole spectrometer. A backward event was defined by the requirement that all vertex tracks pointed in the direction opposite to the LHCb dipole spectrometer. Mixed events were defined as the remaining events (i.e. with at least one of the vertex tracks in each direction). Figure 10 shows the distribution of forward, backward and mixed events in e-e crossings for fill 1089 (see the appendix for the other relevant fills). For LHCb, the Bunch Crossing ID (BCID) is associated to the RF bucket of Beam1 by the relation RF bucket =  $10 \cdot \text{BCID} - 9$ . For Beam2 the correspondig RF bucket is  $10 \cdot (\text{BCID} - 894) - 9$ , modulo 35640. Therefore, for fill 1089,

BCID = 1786 corresponds to the only b-b crossing, BCID = 1 to the only b-e crossing and BCID = 895 to the only e-b crossing. In b-e (e-b) crossings, all events recorded were of the forward (backward) type. In e-e crossings, both forward and backward events were observed, mostly in the “near bunch” positions, i.e.  $\pm 1...3$  slots away from any nominally filled slot. A number of mixed events with tracks in both directions, were recorded in the “near bunch” slots around the b-b crossings. The zoomed plots in figure 10 show the accumulation of events in e-e crossings around the bunch positions and that of mixed type events around the b-b crossing (reminding that the trigger was 100% blocked for BCID = 1787).

Figure 11 shows the  $x$ - $z$  distribution of reconstructed vertices of forward, backward and mixed type in e-e crossings for fill 1089 (see the appendix for the other relevant fills). The mixed events, which are accumulated in the luminous region, are attributed to  $\sqrt{s} = 7$  TeV p-p interactions. Forward and backward events in non-b-b crossings are largely due to Beam1-gas or Beam2-gas interactions respectively, as supported by the BCID distribution and  $x$ - $z$  distribution (the LHCb net crossing angle is clearly visible in figure 11). The rate of possible  $\sqrt{s} = 7$  TeV p-p interactions in “near bunch” slots that could be misidentified as forward or backward was checked on an minimum bias event sample from b-b crossings. About 10% (1%) of these events were identified as forward (backward). A correction was applied to take this observation into account.

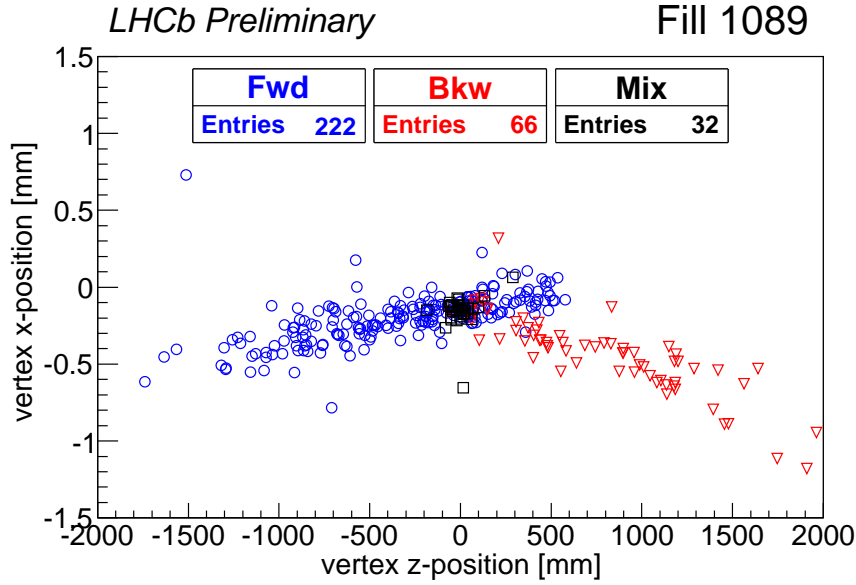


Figure 11: Distribution of reconstructed vertices in e-e crossings in the  $x$ - $z$  plane for fill 1089: forward events (blue circles), backward events (red triangles), mixed events (black squares).

For the example fill 1089, one observes a concentration of ghost charge in the “near bunch” slots. The rest of the ghost charge seems distributed randomly around the ring. The ghost charge in the slot corresponding to BCID = 1787 was not measured and can constitute an important fraction of the total ghost charge. It will be discussed further below.

The number of events measured in the various crossing types are summarized in table 8 for the four van der Meer scan fills. The rates of mixed events are shown in table 8 (column “mixed”) and are compatible with the amount of satellite bunch populations obtained by the methods of ATLAS and CMS described below.

The total ghost fraction for Beam1 (Beam2) was extracted from the number of forward (backward) events measured in e-e crossings divided by the total number of events measured in b-e (e-b) crossings, taking into account the relative populations of the non-colliding and colliding bunches.

For Beam1, the ghost fraction is

$$f_{\text{ghost},1} = \frac{N_{\text{ghost},1}}{N_{\text{tot},1}} = \frac{F_{\text{e-e}}}{F_{\text{b-e}}} \cdot \frac{\sum_{i \in \text{b-e}} S_i}{\sum_{i=1, \dots, n} S_i} \quad (7)$$

Fill number	Events in b-e	Events in e-b	Events in e-e (near bunch)					
			Forward		Backward		Mixed	
1058	11295	7958	31	(17)	7	(6)	3	(3)
1059	1574	1515	4	(4)	0	(0)	0	(0)
1089	12694	12148	222	(97)	66	(42)	32	(30)
1090	6086	4872	52	(31)	44	(39)	31	(30)

Table 8: Beam-gas events measured by LHCb during the four van der Meer scan fills. All recorded b-e (e-b) events were of forward (backward) type. Here, “near bunch” stands for all slots that are  $\pm 1 \dots 3$  slots away from a nominally filled bunch slot. The subsets of events summed over these slots are given in brackets.

where  $F_{e-e}$  and  $F_{b-e}$  are the forward event rates in e-e and b-e crossings.

For Beam2, the ghost fraction is

$$f_{\text{ghost},2} = \frac{N_{\text{ghost},2}}{N_{\text{tot},2}} = \frac{B_{e-e}}{B_{e-b}} \cdot \frac{\sum_{i \in e-b} S_i}{\sum_{i=1, \dots, n} S_i} \quad (8)$$

where  $B_{e-e}$  and  $B_{e-b}$  are the backward event rates in e-e and e-b crossings.

The resulting ghost fractions are shown in table 9.

Fill number	Beam1 ghost fraction $f_{\text{ghost},1} \cdot 10^2$		Beam2 ghost fraction $f_{\text{ghost},2} \cdot 10^2$	
	all slots	(near bunch slots)	all slots	(near bunch slots)
1058	$0.08 \pm 0.01$	$(0.04 \pm 0.01)$	$0.03 \pm 0.01$	$(0.03 \pm 0.01)$
1059	$0.12 \pm 0.06$	$(0.12 \pm 0.06)$	$0.00 \pm 0.03$	$(0.00 \pm 0.03)$
1089	$0.86 \pm 0.06$	$(0.37 \pm 0.04)$	$0.28 \pm 0.03$	$(0.18 \pm 0.03)$
1090	$0.43 \pm 0.06$	$(0.25 \pm 0.05)$	$0.44 \pm 0.07$	$(0.39 \pm 0.06)$

Table 9: Results for the ghost fraction (in percent), as extracted from LHCb beam-gas interaction data. Here, “near bunch” stands for all slots that are  $\pm 1 \dots 3$  slots away from a nominally filled bunch slot. The ghost fractions concentrated in these slots are given in brackets.

It is relevant to point out that this method of ghost charge determination has an intrinsic time granularity of 25 ns. The response to ghost charge in intermediate RF buckets, e.g. satellite bunches at  $\pm 5$  ns from a nominal bunch slot, remains to be understood. Here, we have assumed that the trigger and reconstruction efficiency does not depend on the delay of the interaction relative to the 40 MHz clock ticks. Furthermore, because of the fact that the trigger was most of the time inhibited for the e-e crossings immediately after a b-b crossing, the LHCb results for the ghost charge are slightly underestimating the actual ghost charge. This feature will be avoided in future luminosity calibration experiments. However, the measurements of ATLAS and CMS (see below), which focus on a smaller window around the b-b crossings and with a finer granularity, allow one to “bridge the gap” between the nominally filled bucket and the b-b+2 crossing monitored by LHCb.

The systematic uncertainty on the ghost charge is here dominated by the blocking of the trigger for the BCID following the b-b crossing. Constraints from the ATLAS/CMS displaced collision analyses (see section 4.3.3) and from the distribution of ghost charge around the blocked BCID indicate that the ghost fraction is underestimated by an amount smaller than 0.002.

The LHCb results show an accumulation of ghost charge around the nominally filled RF buckets. Complementary to the LHCb analysis, ATLAS and CMS produced constraints on ghost charge in the neighbourhood of these nominally filled RF buckets, as discussed next.

#### 4.3.2 Satellite bunch populations from precise timing

Charge stored in the neighbourhood of a nominally filled bunch will result in collisions that are displaced in time and along  $z$ . A satellite bunch lagging 5 ns behind the nominally filled bucket (e.g. in RF bucket 3

when the main bunch is in RF bucket 1) will cause p-p interactions with the counter-rotating main bunch at a longitudinal displacement of about  $\Delta z = \pm 75$  cm from the IP, where the  $- (+)$  sign is for a satellite bunch in Beam1 (Beam2). If the late satellite bunch is in Beam1, particles emerging from the displaced collisions will be delayed by 5 ns in a detector located on the right side ( $z > 0$ , i.e. in the outgoing direction of Beam1) of the IP, but in time for a detector located on the left side ( $z < 0$ ), where the arrival time is taken relative to ejectiles from the colliding main bunches at the IP. The 5 ns delay will be seen in the left side detector if the late satellite bunch is in Beam2. Similarly, a satellite bunch preceding by 5 ns the nominally filled bucket (e.g. in RF bucket 35639 when the main bunch is in RF bucket 1) will cause p-p interactions with the counter-rotating main bunch at a longitudinal displacement of about  $\pm 75$  cm from the IP where now the  $-$  and  $+$  are for a satellite bunch in Beam2 and Beam1. In this case, the displaced collisions will produce particles that are advanced by 5 ns in detectors situated on the side of the IP toward which the satellite bunch is moving.

The CMS analysis used the two endcap electromagnetic calorimeters (EE) located on both sides of IP5 (and labeled EEP for  $z < 0$  and EEM for  $z > 0$ ) with minimum bias triggered events. Groups of crystals (clusters) with a seed crystal of energy above 4 GeV were selected to measure the time with high precision. The time resolution for crystals at this energy or higher is less than 1 ns [24].

Figure 12 shows for fill 1089 the reconstructed time of EE clusters relative to the expected reconstructed time from collisions occurring at the nominal time and nominal IP position (see the appendix for the other relevant fills). A cluster at +5 (-5) ns in the EEM system is here interpreted as emerging from a p-p interaction in the crossing of the main bunch of Beam1 and a satellite bunch of Beam2 lagging (leading) by 5ns behind (in front of) the main bunch of Beam2. Similarly, a cluster at +5 (-5) ns in the EEP system is interpreted as emerging from a p-p interaction in the crossing of the main bunch of Beam2 and a satellite bunch of Beam1 lagging (leading) by 5ns behind (in front of) the main bunch of Beam1. Figure 12 reveals the presence of a satellite bunch 5 ns behind the main bunch of both beams for the LHC fill 1089. A signature of satellite bunches at -5 ns and +10 ns are also visible.

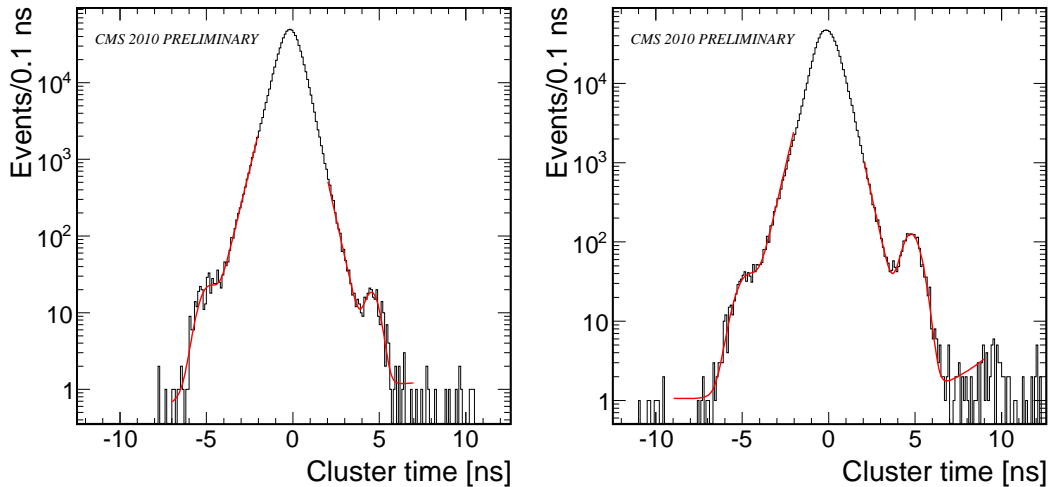


Figure 12: Timing of clusters in the CMS endcap calorimeters for fill 1089: Left: EEP detector (left side of IP,  $z < 0$ ). Right: EEM detector (right side of IP,  $z > 0$ ).

The yields of interactions with clusters delayed by  $\pm 5$  ns in a given endcap calorimeter (“EEM” or “EEP”) were fitted independently with a Gaussian (signal) summed with the exponential of a third order polynome (background). This defined the delayed yield  $R_{\pm 5\text{ns}}$ , which was compared to the on-time yield  $R_{0\text{ns}}$ . The following ratios  $S_{\pm 5\text{ns},0}$  and  $S_{0,\pm 5\text{ns}}$  may be interpreted as a leading or trailing satellite bunch populations (-5 ns or +5 ns respectively) relative to the main bunch population (0 ns), if assuming negligible crossing angle, the same orbits and shapes for all bunches and after correcting for the “hourglass” effect assuming that the rates scale with the inverse of  $\beta(z) = \beta^* \cdot (1 + (z/\beta^*)^2)$  where  $\beta^*$  is the optics function at the IP

(here  $\beta^* \approx 2$  m). Here, the first index in  $S_{\pm 5\text{ns},0}$  and  $S_{0,\pm 5\text{ns}}$  is for Beam1, the second one for Beam2:

$$\begin{aligned} S_{0,+5\text{ns}} &= 2 \left[ \frac{R_{+5\text{ns}}}{R_{0\text{ns}}} \frac{\epsilon_{0\text{ns}}}{\epsilon_{+5\text{ns}}} \frac{A_{0\text{ns}}}{A_{+5\text{ns}}} \right]_{\text{EEM}} & S_{+5\text{ns},0} &= 2 \left[ \frac{R_{+5\text{ns}}}{R_{0\text{ns}}} \frac{\epsilon_{0\text{ns}}}{\epsilon_{+5\text{ns}}} \frac{A_{0\text{ns}}}{A_{+5\text{ns}}} \right]_{\text{EEP}} \\ S_{0,-5\text{ns}} &= 2 \left[ \frac{R_{-5\text{ns}}}{R_{0\text{ns}}} \frac{\epsilon_{0\text{ns}}}{\epsilon_{-5\text{ns}}} \frac{A_{0\text{ns}}}{A_{-5\text{ns}}} \right]_{\text{EEM}} & S_{-5\text{ns},0} &= 2 \left[ \frac{R_{-5\text{ns}}}{R_{0\text{ns}}} \frac{\epsilon_{0\text{ns}}}{\epsilon_{-5\text{ns}}} \frac{A_{0\text{ns}}}{A_{-5\text{ns}}} \right]_{\text{EEP}} . \end{aligned} \quad (9)$$

The ratio of  $A_{0\text{ns}}/A_{+(-)5\text{ns}}$  accounts for the difference in acceptance for collisions closer or farther to the detector, namely for collisions 75 cm closer to (farther from) the detector. The ratio  $1.205 \pm 0.07$  ( $0.61 \pm 0.07$ ) was used. The ratio  $\epsilon_{0\text{ns}}/\epsilon_{+(-)5\text{ns}}$  accounts for a difference in selection efficiency due to amplitude reconstruction bias for late hits, and the value  $1.058 \pm 0.02$  was used (no correction is required for the 5 ns early hits). Acceptance and reconstruction efficiency ratios were obtained with data driven techniques. To estimate the acceptance change in the endcap calorimeter when displacing the collision point, first the new pseudorapidity range subtended by an endcap for a displaced collision was calculated from geometrical arguments. The pseudorapidity is defined as  $\eta = -\ln(\tan \frac{\theta}{2})$ , where  $\theta$  is the polar angle from the  $z$  axis. Then the  $\eta$  range on either sides of the coverage for nominal collisions was extended, using the barrel detector on one side (lower  $|\eta|$ ) and a continuous extrapolation of the experimental distribution on the other (higher  $|\eta|$ ). Finally, using the thus extended  $\eta$  distribution of the clusters, the number of clusters in the new  $\eta$  range was compared with the one in the nominal  $\eta$  range. To estimate the efficiency change, the variation of the reconstructed amplitude with time displacements is known for the  $\pm 5$  ns case [25]. To obtain the efficiency, the analysis cuts were varied in the amplitude spectra and the ratios of the resulting yields were calculated. Furthermore, the trigger efficiency was assumed to be the same for all interactions in the range of interest. The satellite bunch population fractions were corrected for the larger size of the beam at  $|z| > 0$  assuming a  $\beta^*$  value of 2 m.

For direct comparison with the vertexing methods presented below, the signals at a displacement of  $\pm 75$  cm are here calculated from

$$S_{+75\text{cm}} = S_{-5\text{ns},0} + S_{0,+5\text{ns}} \quad \text{and} \quad S_{-75\text{cm}} = S_{0,-5\text{ns}} + S_{+5\text{ns},0} . \quad (10)$$

Under these assumptions, the results for the relative satellite population at  $\pm 5$  ns are shown in table 10 for the four van der Meer scan fills.

Fill	$S_{+5\text{ns},0} \cdot 10^3$	$S_{0,-5\text{ns}} \cdot 10^3$	$S_{-75\text{cm}} \cdot 10^3$
1058	$< 0.007$	$< 0.013$	$< 0.021$
1059	$< 0.079$	$< 0.127$	$< 0.206$
1089	$1.53 \pm 0.068 \pm 0.26$	$0.390 \pm 0.053 \pm 0.066$	$1.919 \pm 0.086 \pm 0.326$
1090	$0.498 \pm 0.103 \pm 0.085$	$0.225 \pm 0.077 \pm 0.038$	$0.724 \pm 0.123 \pm 0.123$
	$S_{-5\text{ns},0} \cdot 10^3$	$S_{0,+5\text{ns}} \cdot 10^3$	$S_{+75\text{cm}} \cdot 10^3$
1058	$< 0.040$	$< 0.004$	$< 0.044$
1059	$< 0.085$	$< 0.068$	$< 0.152$
1089	$0.828 \pm 0.152 \pm 0.141$	$0.155 \pm 0.025 \pm 0.026$	$0.983 \pm 0.154 \pm 0.167$
1090	$0.270 \pm 0.103 \pm 0.046$	$0.175 \pm 0.048 \pm 0.030$	$0.446 \pm 0.144 \pm 0.076$

Table 10: CMS results for the  $\pm 5$  ns (trailing/leading) satellite bunch population relative to the main bunch. The first uncertainty is statistical, the second is systematic.

#### 4.3.3 Satellite bunch populations from vertexing

ATLAS and CMS performed a study based on the reconstruction of longitudinally displaced vertices. Because of the zero crossing angle, satellite bunches collided with the main bunches at precise locations outside the nominal luminous region. The ATLAS analysis used a loose vertex reconstruction algorithm covering a broad range in  $z$ . It retained one primary vertex per crossing, defined as the one with the largest sum of the squared transverse momenta of the tracks assigned to each vertex. The vertex reconstruction



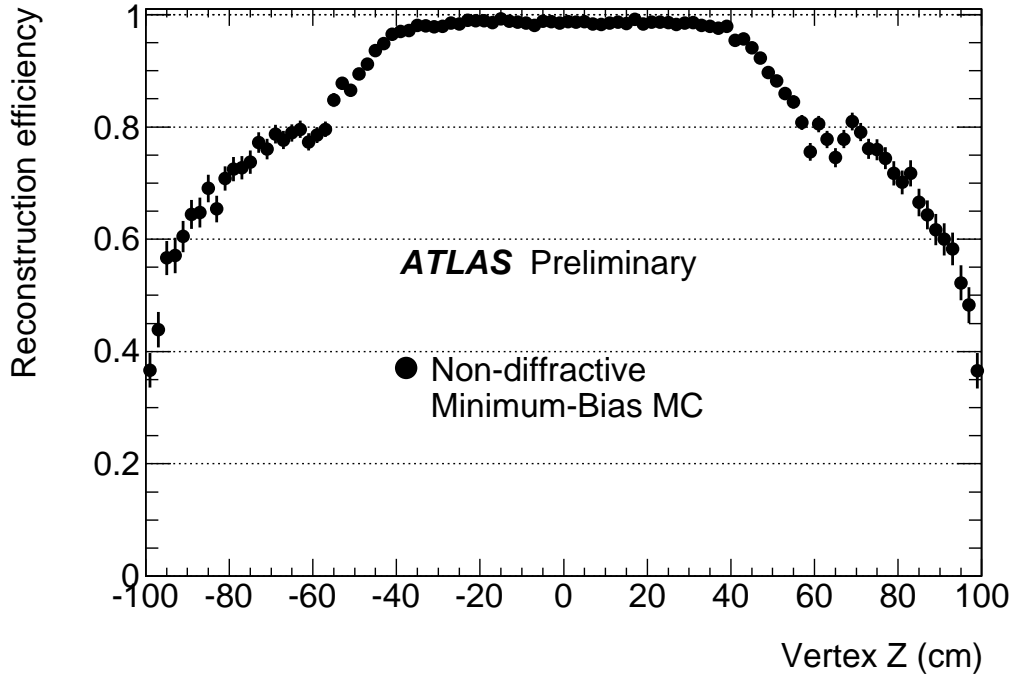


Figure 13: ATLAS primary vertex reconstruction efficiency for the loose vertex reconstruction algorithm used in this work, shown as a function of  $z_{\text{vtx}}$ , as obtained from a Monte-Carlo simulation.

efficiency was estimated by a Monte-Carlo simulation and is shown in figure 13 as a function of  $z_{\text{vtx}}$ . The  $z$  vertex resolution was in the order of 0.1 mm.

Figure 14 shows the ATLAS primary vertex distribution for fill 1089, after correcting for the vertex reconstruction efficiency (see the appendix for the other relevant fills). The central peak is due to interactions from the colliding main bunches. Two additional peaks are clearly visible at  $z \approx \pm 75$  cm and are attributed to interactions from the crossing of the main bunches with a satellite bunch displaced by  $\pm 5$  ns relative to the main bunch. Note that this method alone cannot discriminate between a trailing satellite in Beam2 colliding with the main bunch of Beam1 and a leading satellite in Beam1 colliding with the main bunch of Beam2 (or vice versa): both give rise to displaced collisions at  $z \approx +75$  cm (respectively,  $-75$  cm).

The vertex distributions were fitted with a sum of four Gaussian curves (one for the background, one for the main peak and one for each of the peaks around  $\pm 75$  cm). The maximum spread of the measured background rate in the four fills analyzed has been taken as systematic uncertainty on its prediction. The rate above background in a given  $z$  bin around a selected  $z$  value was used as a measure of the relative luminosity at the associated  $z$ . The relative amplitudes of (or upper limits on) the different peaks  $S_z$  (here  $z = \pm 75$  cm) were determined from these rates.

$$S_z = \frac{R_z}{R_{0\text{cm}}} \frac{\epsilon_{0\text{cm}}}{\epsilon_z} \quad (11)$$

where  $R_z$  and  $\epsilon_z$  represent the reconstructed rate and reconstruction efficiency for interactions at  $z$ .

The CMS analysis was based on an algorithm using the silicon tracker endcap wheels. This gave a broader  $z_{\text{vtx}}$  acceptance, although with reduced  $z$  resolution compared to the barrel tracker for the nominal luminous region. The analysis was carried out separately for the two sides of the tracker (the “M” side and “P” side, which in the current work correspond to detectors located at  $z > 0$  and  $z < 0$  respectively). Figure 15 shows the reconstructed vertex distribution for the M and P side, respectively, for fill 1089 before correcting for vertex reconstruction efficiency (see the appendix for the other relevant fills). The reconstruction efficiency as a function of  $z$ , shown in figure 16, was estimated from Monte-Carlo simulations.

Each side produces an independent result for the amount of interactions at a given  $z$ . The  $S_z$  values were calculated for each  $z$  from the weighted average of the two results. In this CMS analysis, results for  $z =$



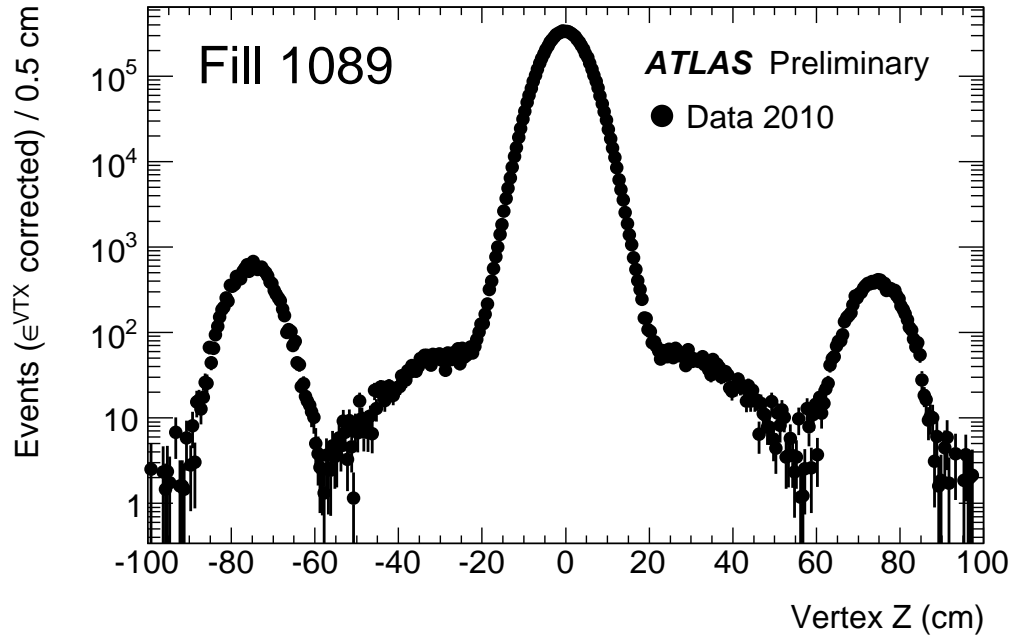


Figure 14: ATLAS primary vertex distribution as a function of  $z_{\text{vtx}}$  for fill 1089, after correcting for vertex reconstruction efficiency.

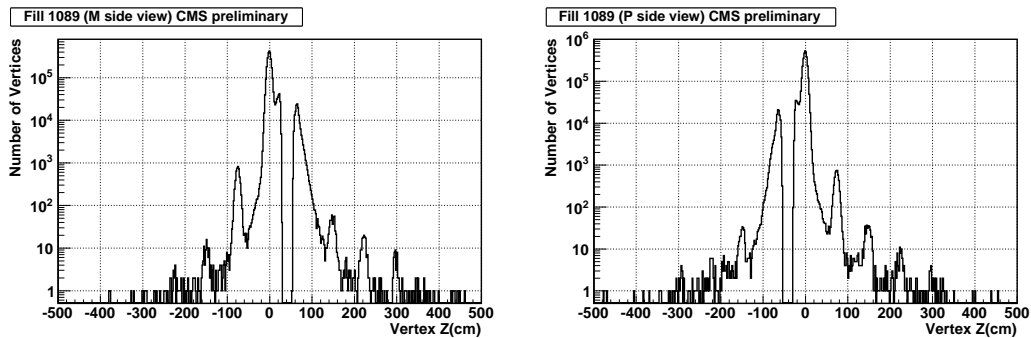


Figure 15: CMS vertex distribution as a function of  $z$  for fill 1089, before correcting for vertex reconstruction efficiency, using the M side (left graph) or the P side (right graph) of the tracker.

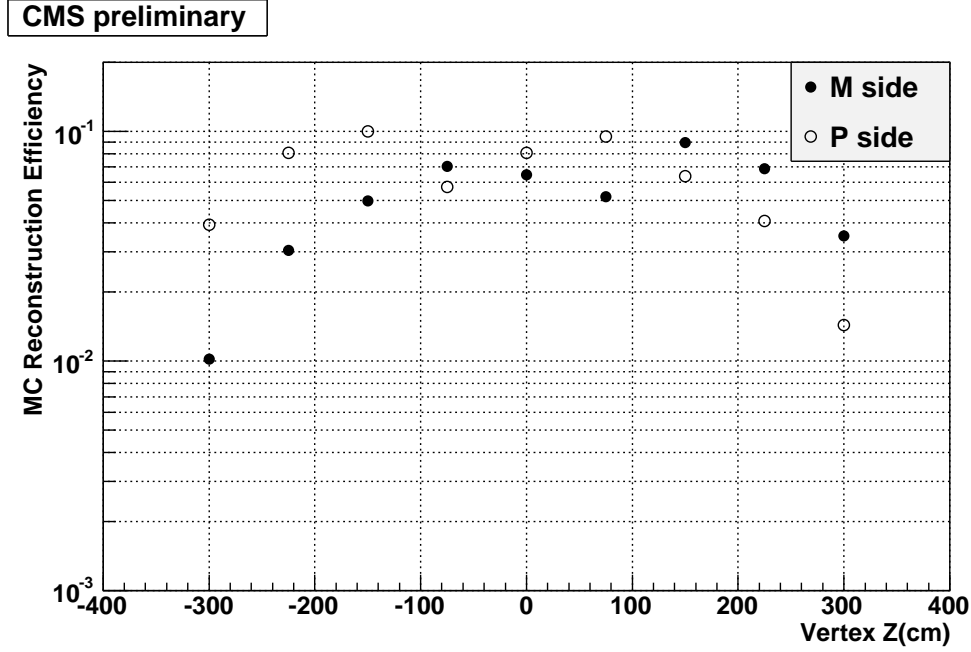


Figure 16: CMS vertex reconstruction efficiency as a function of  $z$  (derived from Monte-Carlo simulations) for the algorithm discussed in the text.

$\pm 75$ , 150, 225 and 300 cm were produced. ATLAS produced results for  $z = \pm 37.5$ , 75 cm. Both the ATLAS and CMS values were corrected for the larger size of the beam at  $|z| > 0$  assuming  $\beta^*$  of 2 m (up to 14% upward corrections for ATLAS and up to a factor 3.25 increase for the CMS values at  $z = \pm 300$  cm). The ATLAS values were also corrected for pile-up interactions (up to 5% upward corrections).

The ATLAS and CMS results for the four van der Meer scan fills are shown in table 11. For all these runs no significant satellite contribution at  $\pm 37.5$  cm is observed. This allows one to place bounds of about  $10^{-4}$  times the main peak, limited by the uncertainties on the prediction of the background rate. The uncertainties on  $s_z$  include those from background estimation, vertex reconstruction efficiency and the statistical uncertainties. No systematic uncertainty on general Monte-Carlo modeling was applied (only the statistical Monte-Carlo uncertainty was used). The ATLAS results are discussed in more details elsewhere [26].

#### 4.3.4 Summary on ghost charge and satellite bunches

The total level of ghost charge reached a value close to 1% for Beam1 in LHC fill 1089. It was smaller for Beam2 and in general for the other April-May 2010 van der Meer scan fills. The LHCb measurements from beam-gas rates indicate about equal contributions from charge distributed evenly around the ring and from charge around the nominally filled bunch slots.

The results of the ATLAS and CMS analyses of displaced interaction regions are consistent and indicate satellite populations of up to about 0.2% for fill 1089. For this fill, CMS vertexing data indicate that satellite populations in buckets at  $\pm 10$ , 15 and 20 ns from the main bunches were an order of magnitude smaller than for the buckets at  $\pm 5$  ns. The satellite bunch populations are quoted as fractions of the main bunch colliding at IP1 and IP5. The charge at 5 ns steps from the main bunches was likely due to satellite bunches coming from the injector (SPS) which works with 200 MHz cavities. For the vertexing results, the quoted values are the sum of a trailing bunch in one beam and a leading bunch in the other beam. The CMS timing measurements indicate that the trailing satellite populations were dominant. When summing the trailing/leading satellite contributions, the CMS timing results are in agreement with the results of the ATLAS and CMS vertexing analysis.

If one assumes equal satellite distribution around all nominally filled bunches, the total fraction in the

Satellite bunch fractions $\mathcal{S}_z \cdot 10^3$ at different $z$						
Fill		$\mathcal{S}_{-300\text{cm}} \cdot 10^3$	$\mathcal{S}_{-225\text{cm}} \cdot 10^3$	$\mathcal{S}_{-150\text{cm}} \cdot 10^3$	$\mathcal{S}_{-75\text{cm}} \cdot 10^3$	$\mathcal{S}_{-37.5\text{cm}} \cdot 10^3$
1058	CMS	-	-	-	$< 0.08$	-
	ATLAS	-	-	-	$< 0.039$	$< 0.089$
1059	CMS	-	-	-	$< 0.06$	-
	ATLAS	-	-	-	$< 0.039$	$< 0.091$
1089	CMS	$0.041 \pm 0.010$	$0.033 \pm 0.007$	$0.080 \pm 0.016$	$2.09 \pm 0.42$	-
	ATLAS	-	-	-	$2.08 \pm 0.18$	$< 0.12$
1090	CMS	$0.021 \pm 0.005$	$0.183 \pm 0.039$	$0.136 \pm 0.028$	$0.99 \pm 0.20$	-
	ATLAS	-	-	-	$0.909 \pm 0.082$	$< 0.1$
Fill		$\mathcal{S}_{+37.5\text{cm}} \cdot 10^3$	$\mathcal{S}_{+75\text{cm}} \cdot 10^3$	$\mathcal{S}_{+150\text{cm}} \cdot 10^3$	$\mathcal{S}_{+225\text{cm}} \cdot 10^3$	$\mathcal{S}_{+300\text{cm}} \cdot 10^3$
1058	CMS	-	$< 0.07$	-	-	-
	ATLAS	$< 0.089$	$< 0.039$	-	-	-
1059	CMS	-	$< 0.05$	-	-	-
	ATLAS	$< 0.091$	$< 0.039$	-	-	-
1089	CMS	-	$1.50 \pm 0.30$	$0.192 \pm 0.039$	$0.106 \pm 0.022$	$0.108 \pm 0.026$
	ATLAS	$< 0.13$	$1.55 \pm 0.13$	-	-	-
1090	CMS	-	$0.67 \pm 0.14$	$0.170 \pm 0.036$	$0.096 \pm 0.022$	$0.026 \pm 0.012$
	ATLAS	$< 0.12$	$0.585 \pm 0.056$	-	-	-

Table 11: CMS and ATLAS results on satellite bunch populations from vertexing of the displaced collisions relative to the IP.

satellites (within  $\pm 20$  ns), could have reached up to 0.4% of the beam current in the worst case (fill 1089). The population of satellites outside  $\pm 12.5$  ns is constrained by the LHCb beam-gas rates.

## 5 Discussion and summary

In this work we reported on an analysis of the bunch current data relevant for the luminosity normalization of the April-May 2010 calibration experiments at the LHC. The determination of the bunch population contributing to luminosity was determined from the FBCT signals, the sum of which was normalized to the total current measured by the DCCT after subtracting the ghost charge. The amount of ghost charge was determined from measurements by the detectors of the LHC experiments and reached up to 0.85% for one beam in the worst case (fill 1089) as summarized in table 9.

Three main sources of uncertainties on the bunch populations were identified:

- The uncertainties from the DCCT baseline variations are given in table 6 as peak-to-peak bounds  $\Delta N_{\text{tot},1}$  (Beam1) and  $\Delta N_{\text{tot},2}$  (Beam2). In the preliminary analysis, the DCCT current offset variations of the two beams were conservatively estimated and treated as correlated uncertainties. The results presented in this work indicate that the DCCT variations were smaller than originally estimated in the preliminary analysis and that they can be treated as uncorrelated between the two LHC rings and from fill to fill.
- The uncertainties  $\Delta\alpha$  on the DCCT scale factors were discussed in section 4.1.2. The same peak-to-peak bound was used for both the preliminary and detailed analyses. The uncertainties on the DCCT scale factors might be partly correlated between the two rings. The contributions of the two beams were (conservatively) added linearly. For similar reasons, and until a better understanding of the scale factor uncertainties is obtained, they should also be treated (conservatively) as correlated uncertainties between two fills.

- The relative uncertainties from the FBCT relative bunch population determination were discussed in section 4.2. In the preliminary analysis the FBCT relative bunch population uncertainties were neglected, while in the detailed analysis they were estimated from a comparison to the ATLAS BPTX signals and included in the overall uncertainties. This systematic uncertainty is treated as being uncorrelated between the two beams, but (conservatively) as correlated from fill to fill until a better understanding of the offset and linearity is obtained.

In the preliminary analysis, the total uncertainties on the bunch products were calculated from the linear sum of the DCCT baseline and scale factor contributions. In the detailed analysis presented here, the three above uncertainties were added in quadrature. The ghost charge was taken into account in the detailed analysis and neglected in the preliminary analysis. Its uncertainties contribute negligibly to the total uncertainty.

For the preliminary analysis, as explained in section 4.1.1.1, the uncertainties were finally expressed as standard deviations, see (5), assuming uniform error distributions (i.e. 57.7% confidence level). In what follows, for the final results of the detailed analysis, we use bunch population uncertainties and bunch population product uncertainties corresponding to a 68.2% confidence level, again assuming uniform error distributions.

Preliminary analysis	Detailed analysis (this work)
$\frac{\sigma_{P_{ij}}^{\text{baseline}}}{P_{ij}} = \frac{1}{\sqrt{3}} \left( \frac{\Delta N_{\text{tot},1}}{N_{\text{tot},1}} + \frac{\Delta N_{\text{tot},2}}{N_{\text{tot},2}} \right)$	$\frac{\sigma_{P_{ij}}^{\text{baseline}}}{P_{ij}} = 0.682 \cdot \sqrt{\left( \frac{\Delta N_{\text{tot},1}}{N_{\text{tot},1}} \right)^2 + \left( \frac{\Delta N_{\text{tot},2}}{N_{\text{tot},2}} \right)^2}$
$\frac{\sigma_{P_{ij}}^{\text{scale}}}{P_{ij}} = \frac{2}{\sqrt{3}} \frac{\Delta \alpha}{\alpha} = 2.3\%$	$\frac{\sigma_{P_{ij}}^{\text{scale}}}{P_{ij}} = 0.682 \cdot 2 \cdot \frac{\Delta \alpha}{\alpha} = 2.7\%$
$\frac{\sigma_{P_{ij}}^{\text{FBCT}}}{P_{ij}} = 0$	$\frac{\sigma_{P_{ij}}^{\text{FBCT}}}{P_{ij}} = 0.682 \cdot \sqrt{\left( \frac{\Delta N_{i,1}}{N_{i,1}} \right)^2 + \left( \frac{\Delta N_{j,2}}{N_{j,2}} \right)^2} = 2.9\%$
$\sigma_{P_{ij}} = \sigma_{P_{ij}}^{\text{baseline}} + \sigma_{P_{ij}}^{\text{scale}}$	$\sigma_{P_{ij}} = \sqrt{(\sigma_{P_{ij}}^{\text{baseline}})^2 + (\sigma_{P_{ij}}^{\text{scale}})^2 + (\sigma_{P_{ij}}^{\text{FBCT}})^2}$

Table 12: Summary of the treatment of uncertainties for the preliminary and detailed analyses.

Explicitly, defining  $P_{ij} = N_{i,1} N_{j,2}$  as the population product for bunch  $i$  of Beam1 and bunch  $j$  of Beam2, the uncertainties  $\sigma_{P_{ij}}$  of  $P_{ij}$  were treated as shown in table 12. The results of the bunch populations and bunch population products are summarized in table 13. Each bunch population is tabulated separately with its absolute uncertainty. The relevant bunch population products are given per IP and with the uncertainties calculated as described above. Note that the values given for the bunch population products are averages over the length of the van der Meer scans (as given in table 1) and the following approximation was used

$$\langle P_{ij} \rangle = \langle N_{i,1} N_{j,2} \rangle \approx \langle N_{i,1} \rangle \langle N_{j,2} \rangle ,$$

an approximation which introduces errors of less than 0.1%. The relative uncertainties on the bunch population products range from 4.4 to 5.6% for the detailed analysis presented in this work (at 68% confidence level), while the standard deviations of the preliminary analysis ranged from 8 to 14%. The reduction of the uncertainties stems primarily from the detailed analysis of the DCCT baseline correction and associated uncertainties, see table 6.

Finally, it is worth pointing out that the results given for the population products at the various IPs are not totally uncorrelated. First, they are all at least partially correlated via the scale factor uncertainty. Second, the measurements in fill 1089 for ATLAS and CMS used the same bunch pairs and are therefore fully correlated (neglecting small changes during the period of the two van der Meer scan experiments). Third, given the fact the FBCT signals were normalized to the total current, the measurements in fill 1059 for ATLAS and LHCb are also subject to an anti-correlation between the populations of the bunches colliding in IP1 and those colliding in IP8.

		Fill number			
		1058	1059	1089	1090
Populations $N \cdot 10^{-9}$					
Beam1	$N(1)$	$9.56 \pm 0.29$ ( $9.42 \pm 0.36$ )	$8.98 \pm 0.34$ ( $8.85 \pm 0.55$ )	$18.99 \pm 0.54$ ( $19.01 \pm 0.62$ )	$19.91 \pm 0.57$ ( $20.00 \pm 0.66$ )
	$N(8941)$	$11.70 \pm 0.35$ ( $11.53 \pm 0.44$ )	- -	- -	- -
	$N(17851)$	$11.02 \pm 0.33$ ( $10.85 \pm 0.41$ )	$10.20 \pm 0.38$ ( $10.05 \pm 0.62$ )	$19.08 \pm 0.54$ ( $19.09 \pm 0.62$ )	$17.33 \pm 0.50$ ( $17.40 \pm 0.57$ )
Beam2	$N(1)$	$10.19 \pm 0.31$ ( $9.56 \pm 0.40$ )	$10.35 \pm 0.37$ ( $10.30 \pm 0.59$ )	$22.18 \pm 0.61$ ( $22.34 \pm 0.64$ )	$19.54 \pm 0.55$ ( $19.34 \pm 0.60$ )
	$N(8911)$	$10.66 \pm 0.33$ ( $10.00 \pm 0.42$ )	$10.35 \pm 0.37$ ( $10.30 \pm 0.59$ )	$21.20 \pm 0.59$ ( $21.36 \pm 0.62$ )	$20.88 \pm 0.59$ ( $20.66 \pm 0.64$ )
	$N(17851)$	$9.43 \pm 0.29$ ( $8.85 \pm 0.37$ )	- -	- -	- -
Population products $P_{ij} \cdot 10^{-18} = N_{i,1} \cdot N_{j,2} \cdot 10^{-18}$					
IP1&5	$N(1) \cdot N(1)$	$97.5 \pm 4.6$ ( $90.0 \pm 9.0$ )	$92.9 \pm 5.2$ ( $91.1 \pm 12.8$ )	$421.1 \pm 18.5$ ( $424.6 \pm 33.8$ )	$389.0 \pm 17.3$ ( $386.6 \pm 32.0$ )
	$N(17851) \cdot N(17851)$	$103.9 \pm 4.9$ ( $96.0 \pm 9.6$ )	- -	- -	- -
IP2	$N(1) \cdot N(8911)$	$101.9 \pm 4.8$ ( $94.2 \pm 9.4$ )	$92.9 \pm 5.1$ ( $91.1 \pm 12.8$ )	$402.7 \pm 17.7$ ( $406.0 \pm 32.4$ )	$415.8 \pm 18.4$ ( $413.2 \pm 34.2$ )
	$N(8941) \cdot N(17851)$	$110.4 \pm 5.2$ ( $101.9 \pm 10.2$ )	- -	- -	- -
IP8	$N(8941) \cdot N(1)$	$119.2 \pm 5.6$ ( $110.1 \pm 11.0$ )	- -	- -	- -
	$N(17851) \cdot N(8911)$	$117.5 \pm 5.5$ ( $108.5 \pm 10.8$ )	$105.6 \pm 5.9$ ( $103.5 \pm 14.5$ )	$404.5 \pm 17.8$ ( $407.9 \pm 32.5$ )	$361.9 \pm 16.0$ ( $359.6 \pm 29.7$ )
Relative errors on population products $\sigma_{P_{ij}}/P_{ij}$					
		4.7% (10%)	5.6% (14%)	4.4% (8%)	4.4% (8.3%)

Table 13: Summary of results from the detailed analysis presented in this work for the bunch populations and bunch population products. Here, the bunches are identified by their nominal RF bucket number  $b$  in bracket  $N(b)$ . The uncertainties are given for 68.2% confidence level. The results given in brackets are those of the preliminary analysis and are standard deviations (57.7% confidence level, see text).

## **6 Acknowledgements**

We would like to thank the CERN management and the LHC Collaborations for their support and encouragements to carry out this work. We also would like to thank our RF colleagues, in particular Philippe Baudrenghien, for the useful discussions on the possible origins of the satellite bunches.

## References

- [1] “*The LHC Machine*”, L. Evans and P. Bryant (editors), JINST **3**, S08001 (2008).
- [2] “*The ALICE Detector at the LHC*”, The ALICE Collaboration, JINST **3**, S08002 (2008).
- [3] “*The ATLAS Detector at the Large Hadron Collider*”, The ATLAS Collaboration, JINST **3**, S08003 (2008).
- [4] “*The CMS Detector at the LHC*”, The CMS Collaboration, JINST **3**, S08004 (2008).
- [5] “*The LHCb Detector at the LHC*”, The LHCb Collaboration, JINST **3**, S08005 (2008).
- [6] For a review, see for example “*Requirements from Precision Physics at LHC on the Luminosity Accuracy*”, S. Tapprogge in “*Forward Physics and Luminosity Determination at LHC*”, editors K. Huitu, V. Khoze, R. Orava, S. Tapprogge (World Scientific Publishing, 2001), and references therein.
- [7] “*Proposal for an absolute luminosity determination in colliding beam experiments using vertex detection of beam-gas interactions*”, M. Ferro-Luzzi, Nucl. Instrum. Methods **A 553**, 388 (2005). <http://cdsweb.cern.ch/record/844569>.
- [8] “*Calibration of the effective beam height in the ISR*”, S. van der Meer, ISR-PO/68-31, 1968 (CERN).
- [9] “*Luminosity scans at HERA*”, G.H. Hoffstaetter, Proc. of EPAC 2002, Paris, France.
- [10] “*Vernier scan results from the first RHIC proton run at 250 GeV*”, K.A. Drees, S.M. White, Proc. IPAC’10, Kyoto, Japan, 23 - 28 May 2010.
- [11] “*Absolute Luminosity from Machine Parameters*”, H. Burkhardt, P. Grafström, LHC-PROJECT-Report-1019 ; CERN-LHC-PROJECT-Report-1019; <http://cdsweb.cern.ch/record/1056691>.
- [12] “*Prompt  $K_S^0$  production in  $pp$  collisions at  $\sqrt{s} = 0.9$  TeV*”, the LHCb Collaboration, R. Aaij *et al*, PLB **693**, 69 (2010); “*Measurement of  $\sigma(pp \rightarrow b\bar{b}X)$  at  $\sqrt{s} = 7$  TeV in the forward region*”, the LHCb Collaboration, R. Aaij *et al*, PLB **694**, 209 (2010).
- [13] See for example in “*First Luminosity Scans in the LHC*”, S.M. White *et al.*, Proc. IPAC’10, Kyoto, Japan, 23 - 28 May 2010; “*Determination of the Luminosity at the LHC Experiments*”, M. Ferro-Luzzi, Proc. of ICHEP2010, Paris, France, 22 - 28 July 2010.
- [14] See for example in “*The luminosity for beam distributions with error and wakefield effects in linear colliders*”, O. Napoly, Part. Acc. **40**, 180 (1993), or in “*Concept of Luminosity*”, W. Herr and B. Muratori, in CAS - CERN Accelerator School: Intermediate Course on Accelerator Physics, Zeuthen, Germany, 15 - 26 Sep 2003, pp.361-378. <http://cdsweb.cern.ch/record/941318>.
- [15] “*Commissioning and First Performance of the LHC Beam Current Measurement Systems*”, D. Belohrad *et al.*, Proc. IPAC’10, Kyoto, Japan, 23 - 28 May 2010.
- [16] “*DCCT TECHNOLOGY REVIEW*”, P. Odier, CARE-Conf-2004-023-HHH, Lyon, December 2004; “*The DCCT for the LHC Beam Intensity Measurement*”, P. Odier *et al.*, DIPAC09, Basel, Switzerland, 25 - 27 May 2009.
- [17] “*On the Measurements of the Beam Current, Lifetime and Decay Rate in the LHC Rings*”, C.Fischer, R.Schmidt, LHC-BCT-ES-0001, EDMS 359172, CERN, Geneva, Switzerland, January 2005.
- [18] “*The 2010 LHC DC BCT measurement system and its main sources of uncertainties*”, P. Odier, J.-J. Gras, M. Ludwig, S. Thoulet, LHC-Project-Note-432, to be published.
- [19] “*Mechanical Design of the Intensity Measurement Devices for the LHC*”, D. Belohrad, P. Odier, S. Thoulet, S. Longo, Proc. DIPAC’07, Venice, Italy, March 2007.
- [20] “*Implementation of the electronics chain for the Bunch by Bunch Intensity Measurement devices for the LHC*”, D. Belohrad, O. R. Jones, M. Ludwig, J. J. Savioz, Proc. DIPAC’09, Basel, Switzerland, May 2009.



- [21] “VME64x Digital Acquisition Board for the LHC Trajectory and Closed orbit System”, R.O. Jones, LHC-BP-ES-0002, EDMS 410295, CERN, Geneva, Switzerland, March 2004.
- [22] “The 2010 LHC ring Fast BCT measurement system and its main sources of uncertainties”, D. Belohrad, J.-J. Gras, M. Ludwig, LHC-Project-Note-433, to be published. “The LHC Fast BCT system: A comparison of Design Parameters with Initial Performance”, D. Belohrad *et al.*, BIW10, Santa Fe, New Mexico, USA, 2 - 6 May 2010.
- [23] “The ATLAS beam pick-up based timing system”, C. Ohm, T. Pauly, Nucl. Instrum. Methods **A 623**, 558 (2010). <http://arxiv.org/abs/0905.3648>.
- [24] “Electromagnetic calorimeter commissioning and first results with 7 TeV data”, The CMS Collaboration, CERN-CMS-NOTE-2010-012, <http://cdsweb.cern.ch/record/1278160>.
- [25] “Reconstruction of the signal amplitude of the CMS electromagnetic calorimeter”, The CMS Electromagnetic Calorimeter Group Eur. Phys. J. C 46, s1.23-s1.35 (2006, DOI: 10.1140/epjcd/s2006-02-002-x).
- [26] “Measurement of the Rate of Collisions from Satellite Bunches for the April-May 2010 LHC Luminosity Calibration”, the ATLAS Collaboration, ATLAS-CONF-2010-102, <http://cdsweb.cern.ch/record/1317334>.

## 7 Appendix

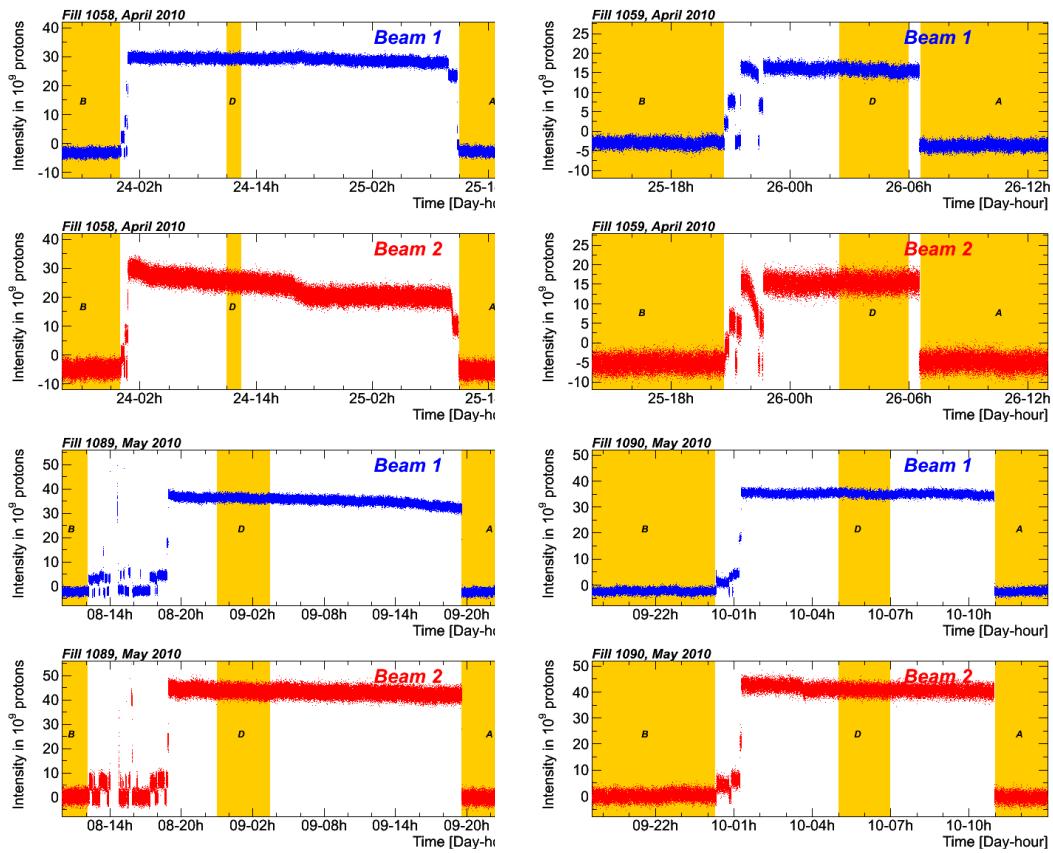


Figure 17: DCCT system B data for the van der Meer scan fills, as retrieved from the LHC logging database. The periods “before”, “during” and “after” the scans used to determine the beam currents are indicated by the shaded bands B, D and A.

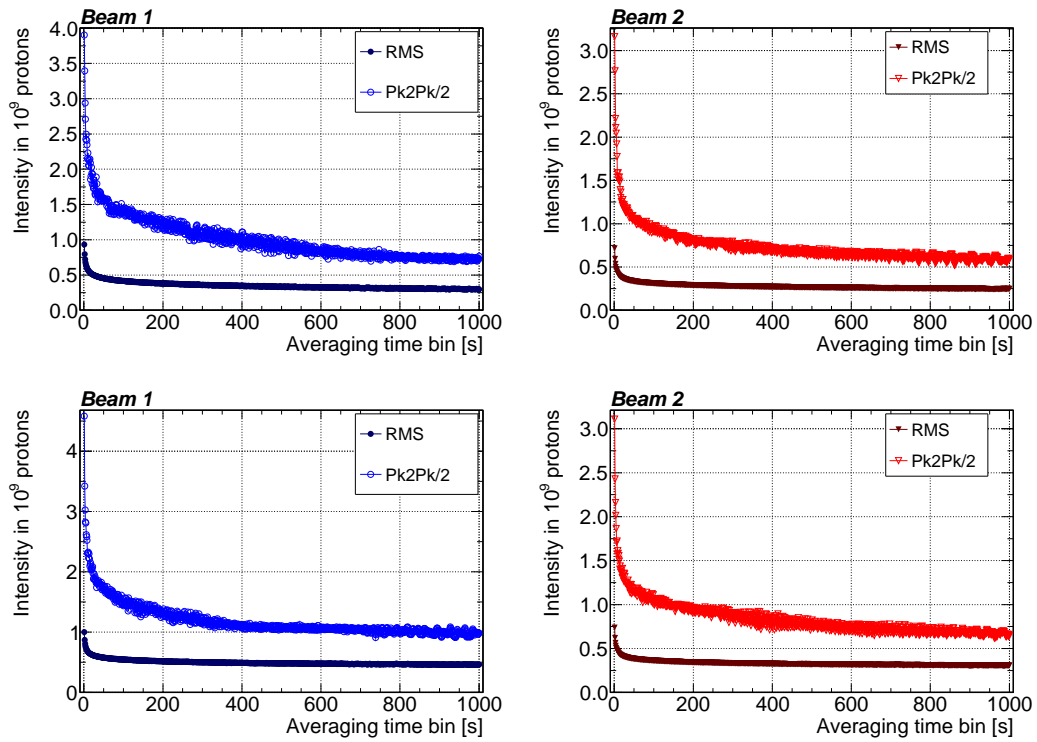


Figure 18: Background period without beam for 26/27 (top) and 27/28 (bottom) April 2010 for Beam1 (left) and Beam2 (right). The RMS (solid symbols) and the peak-to-peak bound (empty symbols) are plotted versus the size of the averaging time bin. The data in the top graphs are identical to those presented in figure 2.

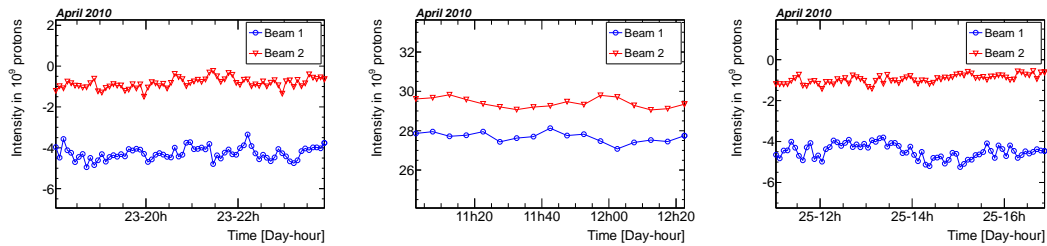


Figure 19: The measured intensity versus time in periods before (left), during (middle) and after (right) a van der Meer scan (fill 1058) for Beam1 (blue circles) and for Beam2 (red triangles), with 300 s averaging time.

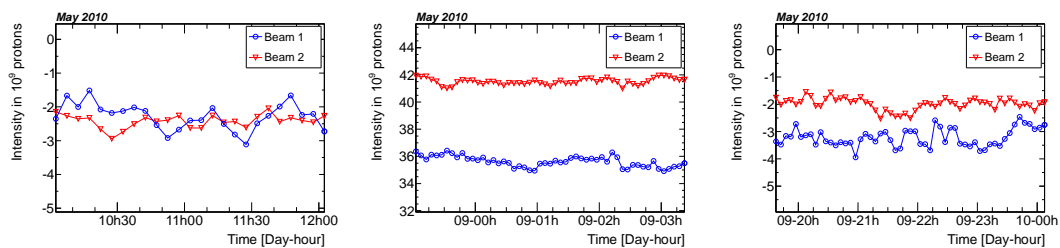


Figure 20: The measured intensity versus time in periods before (left), during (middle) and after (right) a van der Meer scan (fill 1089) for Beam1 (blue circles) and for Beam2 (red triangles), with 300 s averaging time.

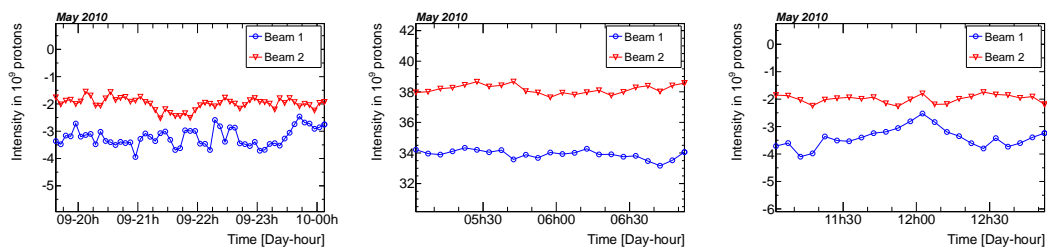


Figure 21: The measured intensity versus time in periods before (left), during (middle) and after (right) a van der Meer scan (fill 1090) for Beam1 (blue circles) and for Beam2 (red triangles), with 300 s averaging time.

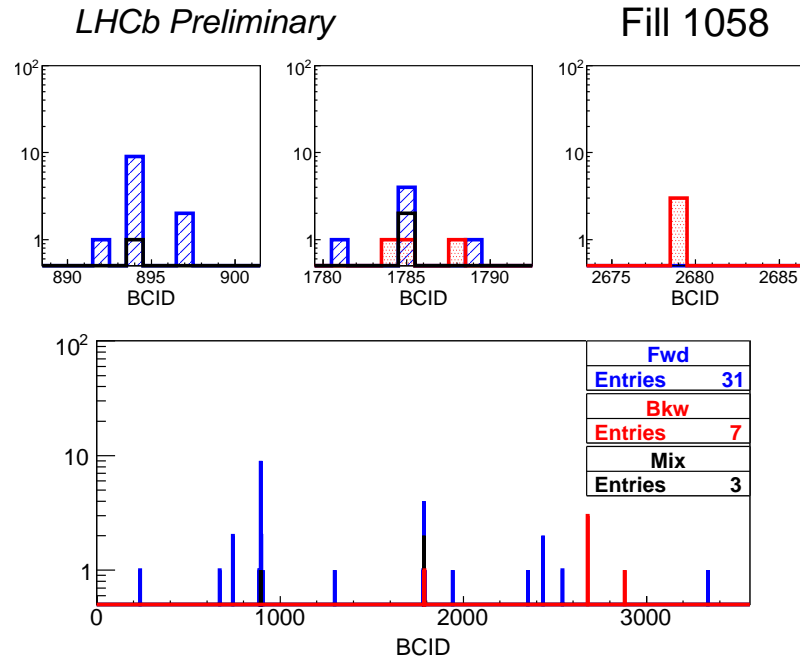


Figure 22: Number of forward (blue, hatched), backward (red, dotted) and mixed (black, empty) events as a function of Bunch Crossing ID for e-e crossings in fill 1058. BCIDs are counted modulo 3564.

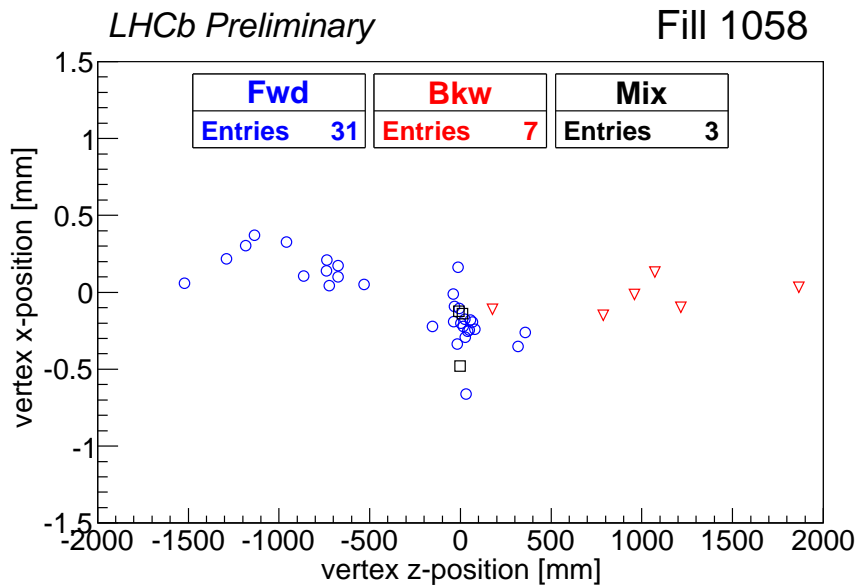


Figure 23: Distribution of reconstructed vertices in e-e crossings in the  $x$ - $z$  plane for fill 1058: forward events (blue circles), backward events (red triangles), mixed events (black squares).

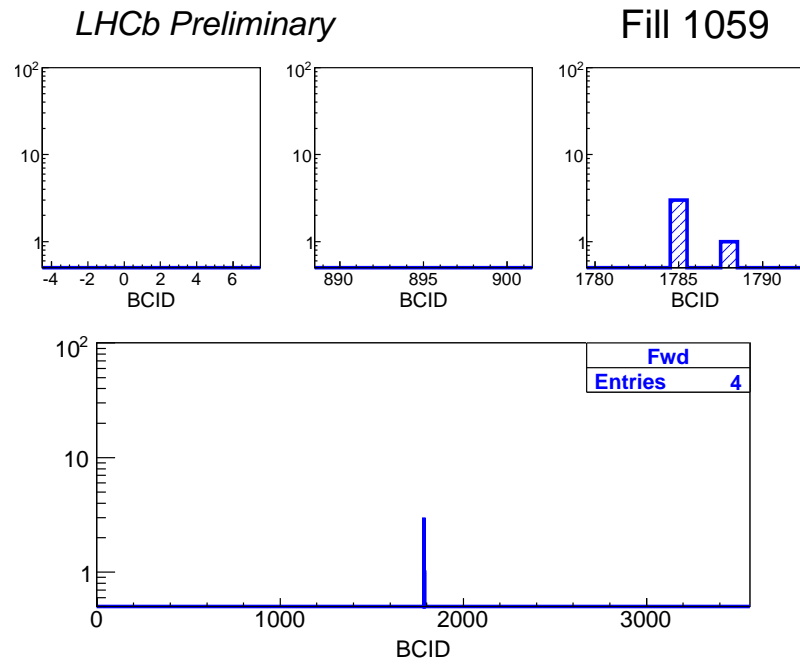


Figure 24: Number of forward (blue, hatched), backward (red, dotted) and mixed (black, empty) events as a function of Bunch Crossing ID for e-e crossings in fill 1059. BCIDs are counted modulo 3564.

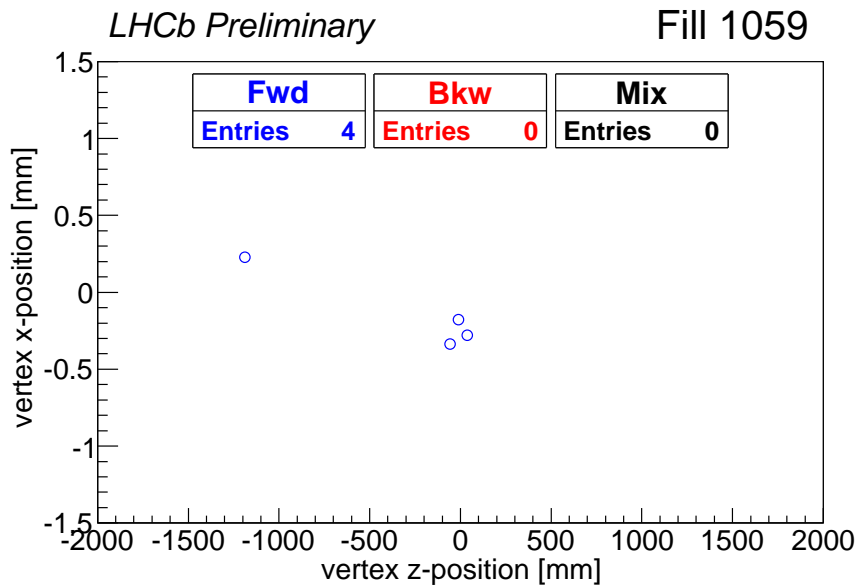


Figure 25: Distribution of reconstructed vertices in e-e crossings in the  $x$ - $z$  plane for fill 1059: forward events (blue circles), backward events (red triangles), mixed events (black squares).

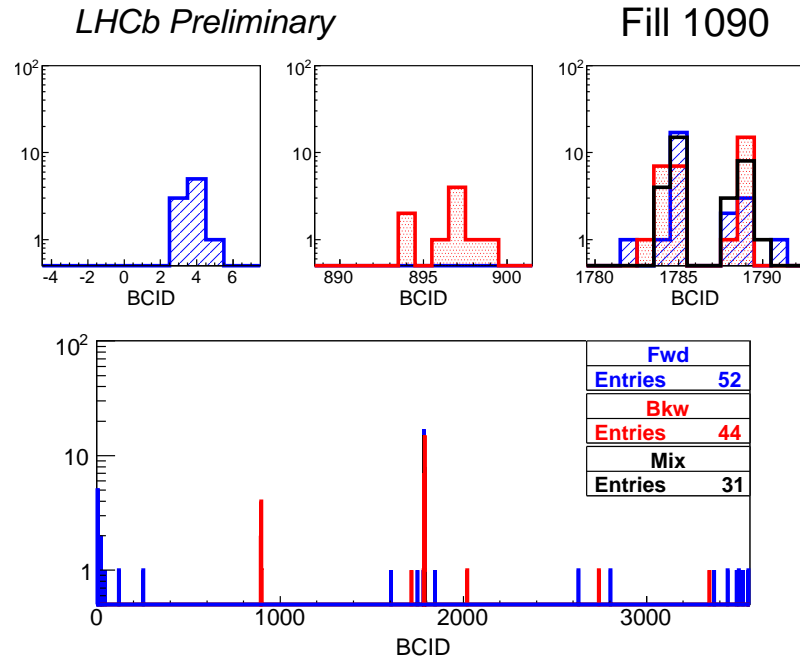


Figure 26: Number of forward (blue, hatched), backward (red, dotted) and mixed (black, empty) events as a function of Bunch Crossing ID for e-e crossings in fill 1090. BCIDs are counted modulo 3564.

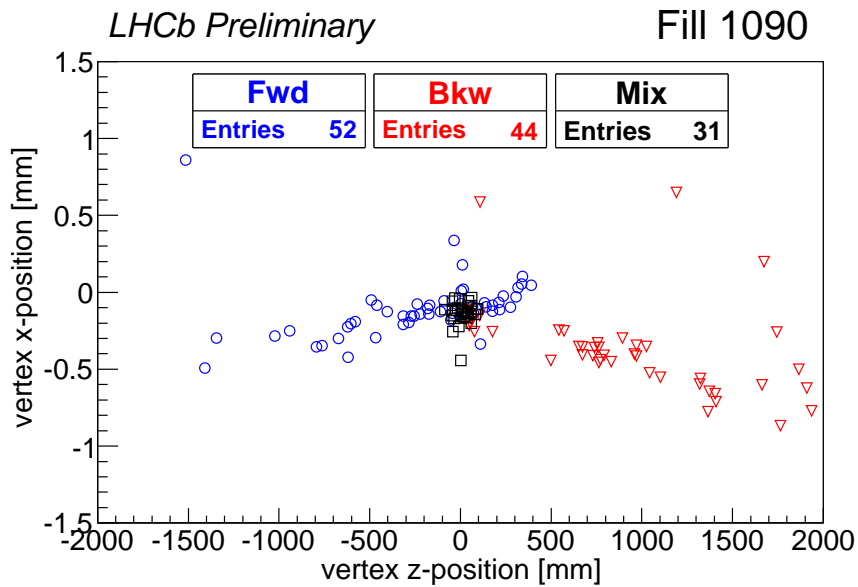


Figure 27: Distribution of reconstructed vertices in e-e crossings in the  $x$ - $z$  plane for fill 1090: forward events (blue circles), backward events (red triangles), mixed events (black squares).



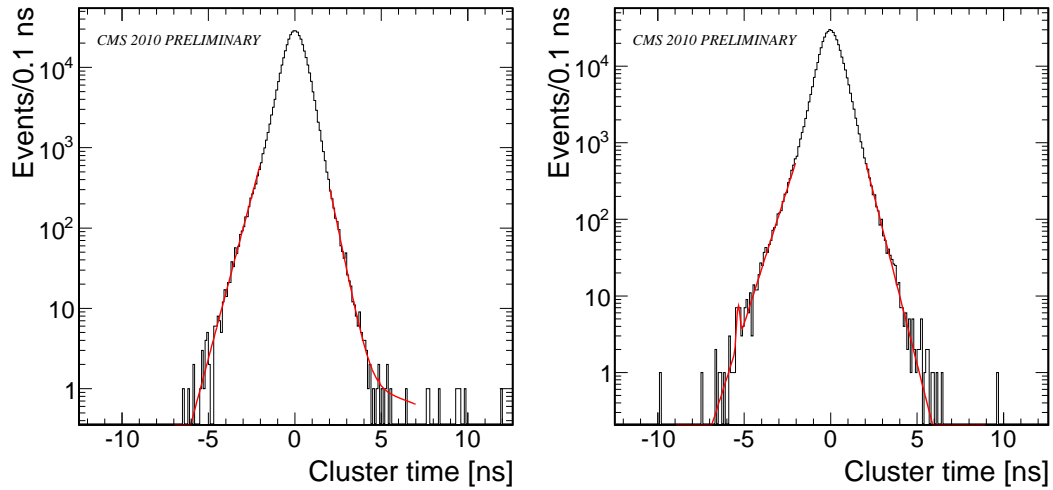


Figure 28: Timing of clusters in the CMS endcap calorimeters for fill 1058: Left: EEP detector (left side of IP,  $z < 0$ ). Right: EEM detector (right side of IP,  $z > 0$ ).

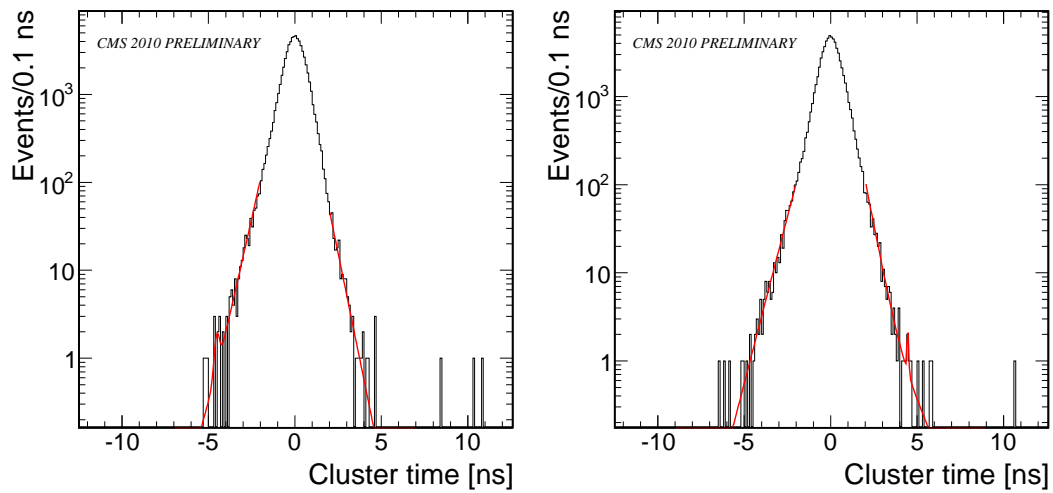


Figure 29: Timing of clusters in the CMS endcap calorimeters for fill 1059: Left: EEP detector (left side of IP,  $z < 0$ ). Right: EEM detector (right side of IP,  $z > 0$ ).

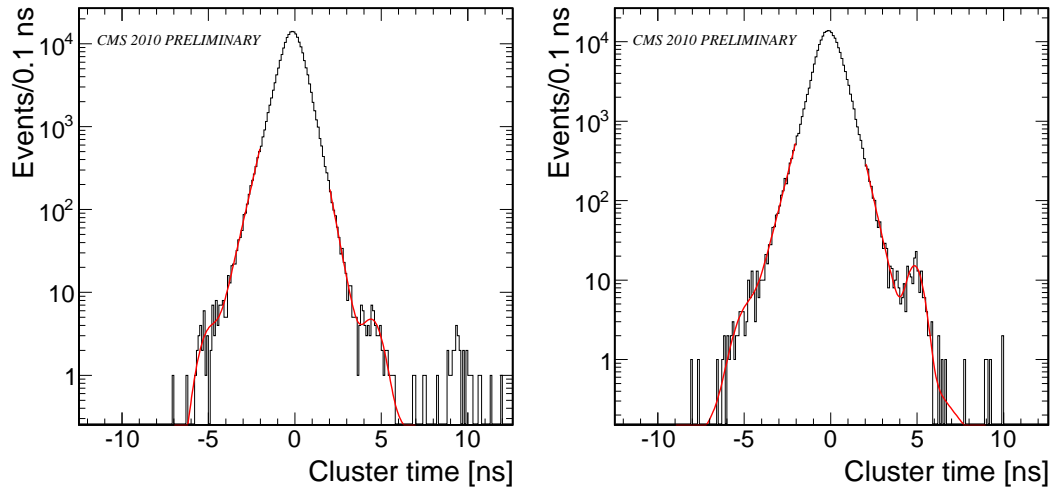


Figure 30: Timing of clusters in the CMS endcap calorimeters for fill 1090: Left: EEP detector (left side of IP,  $z < 0$ ). Right: EEM detector (right side of IP,  $z > 0$ ).

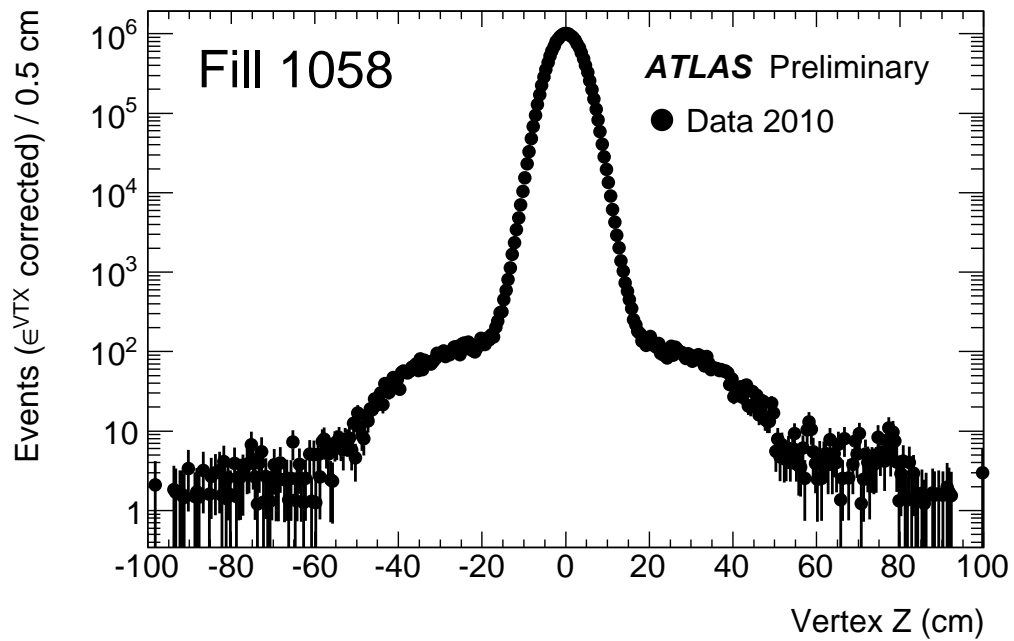


Figure 31: ATLAS primary vertex distribution as a function of  $z_{\text{VTX}}$  for fill 1058, after correcting for vertex reconstruction efficiency.

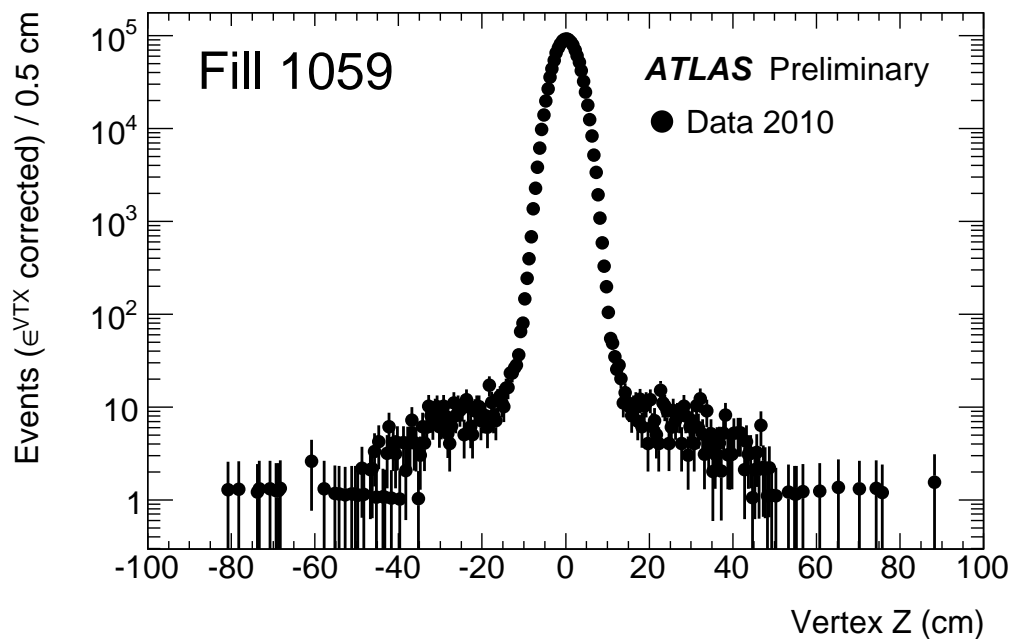


Figure 32: ATLAS primary vertex distribution as a function of  $z_{\text{VTX}}$  for fill 1059, after correcting for vertex reconstruction efficiency.

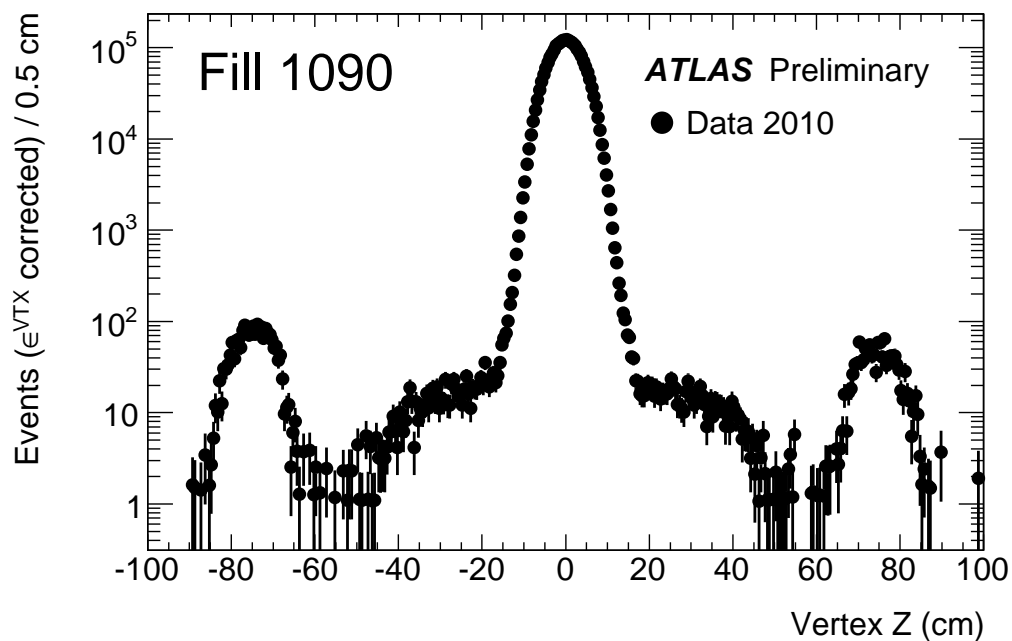


Figure 33: ATLAS primary vertex distribution as a function of  $z_{\text{VTX}}$  for fill 1090, after correcting for vertex reconstruction efficiency.

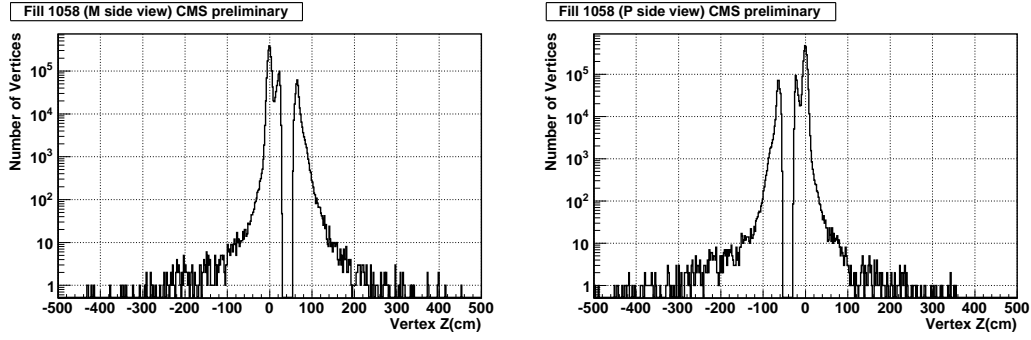


Figure 34: CMS vertex distribution as a function of  $z$  for fill 1058, before correcting for vertex reconstruction efficiency, using the M side (left graph) or the P side (right graph) of the tracker.

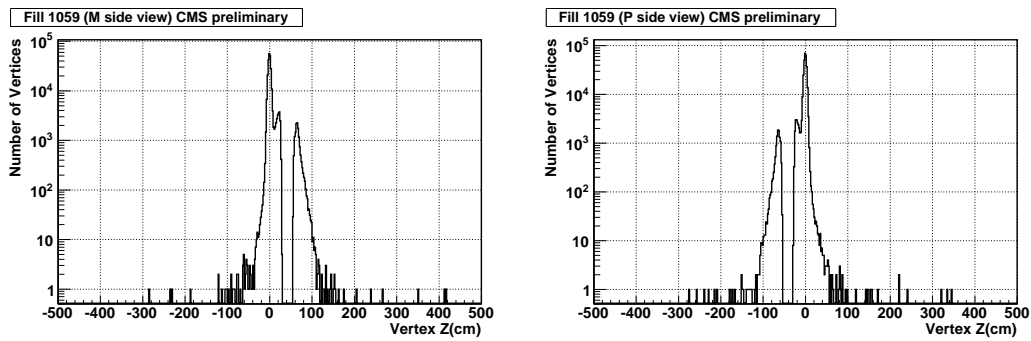


Figure 35: CMS vertex distribution as a function of  $z$  for fill 1059, before correcting for vertex reconstruction efficiency, using the M side (left graph) or the P side (right graph) of the tracker.

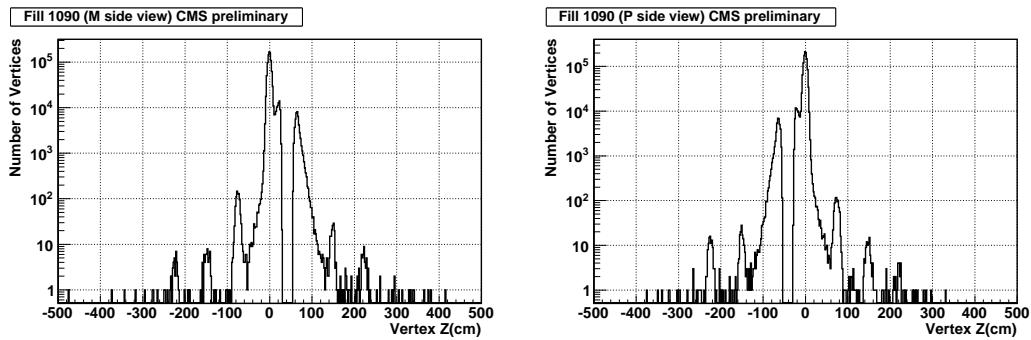


Figure 36: CMS vertex distribution as a function of  $z$  for fill 1090, before correcting for vertex reconstruction efficiency, using the M side (left graph) or the P side (right graph) of the tracker.